GPS Imaging of Mantle Flow-Driven Uplift of the Apennines, Italy

William C. Hammond[1] and Nicola D'Agostino[2]

April 2020

1) Nevada Geodetic Laboratory
Nevada Bureau of Mines and Geology
University of Nevada, Reno
whammond@unr.edu

2) Istituto Nazionale di Geofisica e Vulcanologia
Osservatorio Nazionale Terremoti
Rome, Italy

Key Points:

• A newly updated GPS velocity field reveals uplift of 1-2 mm/yr along the entire length of the Apennines.

• The uplift is aligned with the location of active extension, high topography, seismicity, high gravity, and an upper mantle seismic anomaly.

• These correlations suggest that mantle upwelling contributes to the ongoing increase of elevation and focusing of extensional strain.

Short Title: GPS Imaging Apennine Uplift

Index Terms:
1240: Geodesy and Gravity: Satellite geodesy: results
1213: Geodesy and Gravity: Earth's interior: dynamics
8105: Tectonophysics: Continental margins: divergent
8121: Dynamics: convection currents, and mantle plumes

Abstract

We use a newly updated GPS dataset and the GPS Imaging technique to show that the relief of the Apennines Mountain chain in Italy is currently increasing along its entire length by 1-2 mm/yr. We image positive uplift along the entire length of the Apennine crest including the northern Apennines, Calabria and northern Sicily. The maximum uplift rate is aligned with the topographic drainage divide, the greatest elevations and the zone of horizontal extension accommodating east-northeast translation of the Adriatic microplate relative to the Tyrrhenian Basin. Uplift occurs in a 100 - 150 km wide zone with a profile similar to the long wavelength topography, but not to shorter wavelength topography generated by active faulting and erosion. A zone of lower amplitude uplift aligns with the restive volcanic fields and high geothermal potential west of the Apennines, e.g., at Campi Flegrei, Alban Hills, and Monte Amiata-Larderello. Several factors including consistency of the geodetic rate with geologic uplift rates, and incompatibility with transient hydrological or earthquake cycle effects imply that it is a long-lived feature. Uplift occurs despite that the expected consequence of extension is crustal thinning and subsidence, suggesting a causal relationship between gravitational forces and active extension. Anomalies in gravity and upper mantle seismic velocity suggest that elevation gain is driven by forces originating in the mantle. We use these observations to address the hypothesis that these forces result from upward flow of asthenosphere beneath the Apennines, although the spatial and temporal scale of the mantle circulation is unclear.

Plain Language Summary

We use a newly generated compilation of high-precision geodetic data from hundreds of GPS stations to generate a map of the active uplift that shows the Apennine Mountains of peninsular

Italy currently rising by 1-2 mm/yr. The dataset has greater precision, accuracy and coverage than those previously available. Our analysis focuses on the spatial patterns of the inferred uplift and compares the signals to those in gravity, topography, geomorphic, geologic, and seismic data. We use the data to show that the uplift is representative of solid Earth processes active over geologically relevant periods of time, possibly millions of years, and is related to vertical flow of the Earth's mantle beneath Italy. This active geodynamic process is related to tectonic crustal extension across the Tyrrhenian/Adriatic plate boundary, the evolution of the drainage network, and the presence of hazards from earthquake in the Apennines.

1. Introduction

The topography of Italy south of the Po Plain is dominated by the Apennine mountain chain that extends along the length of the Peninsula from the western Alps in the north to Calabria in the south (Figure 1). The length of the chain is about 500 km, elongated in the NW–SE direction and approximately 100 km wide, occupying about half the width of the Peninsula. The region lies within a plate boundary setting of active north-south convergence between the Eurasian and Nubian plates, where complex Mediterranean tectonics include multiple loci of subduction, extension, and transform tectonics (Faccenna et al., 2014a). The Apennines were most likely formed during Neogene southwest directed subduction of the Adriatic lithosphere beneath the Tyrrhenian lithosphere (Patacca and Scandone, 1989; Serri et al., 1993; Royden et al, 1987) and possibly associated with rollback of the subducting slab that pulled the trench toward the Adriatic (Malinverno and Ryan, 1986). Early Quaternary time saw a marked change in conditions for this plate boundary's dynamic balance, indicated in a record of regional doming of the Apennines and unflexing of the Adriatic plate (Cinque et al., 1993; D'Agostino et al., 2001b;

93 Kruse and Royden, 1994). On the Adriatic side of the Apennines this process interacted with
94 Quaternary eustatic sea level fluctuations and caused the basinward migration of shallow marine
95 deposits, forming an overall prograding system (Ori et al., 1993; Pizzi, 2003). Starting at 2-3 Ma
96 basins developed within central Italy (Martini & Sagri, 1993) coincident with an extensional
97 phase of the axial part of the Apennines that continues to the present day (Cosentino et al., 2017).
98
99 The geological and geomorphological observations, summarized in D'Agostino et al. (2001b),
100 suggest a general doming of the Italian peninsula during the Quaternary on a wavelength larger
101 than 150-200 km. Today, the locus of extension, normal faulting, and seismicity, which drive
102 contemporary generation of local relief, occupy the region with highest elevations and drainage
103 divide of the Apennines (Bartolini et al., 2003; D'Agostino et al., 2001b, 2011). This
104 deformation pattern is consistent with contemporary kinematics of the Adriatic, Tyrrhenian,
105 Nubian, and Eurasia plate motions in the central Mediterranean, which have been charted using
106 geodetic results from regional GPS networks (Bennett et al., 2012; D'Agostino et al., 2008;
107 Devoti et al., 2011; Kreemer et al., 2014; Serpelloni et al., 2005). These studies tend to broadly
108 agree on the overall patterns of translation of the Adriatic to the northeast with respect to Eurasia
109 and the Tyrrhenian lithosphere at a rate of 3-5 mm/yr, driving a zone of extension across the
110 Apennines (D'Agostino, 2014). Vertical geodetic signals are detectible and correlated with
111 topography, but are more difficult to relate directly to geodynamic processes driving elevation
112 growth because the signals have had high noise and contributions from transients that do not
113 necessarily reflect long-term topographic evolution (Bennett et al., 2012; Cenni et al., 2013;
114 D'Anastasio et al., 2006; Devoti et al., 2011; Serpelloni et al, 2013; Silverii et al., 2016). These
115 studies seem to agree, however, that the shallow processes driving seismicity and strain rates in

116 the crust are related to the current configuration of the plate boundary, and are responsible for
117 much of the regional seismic hazard (Stucchi et al., 2011).
118
119 The evolution of Apennine topography has also been connected to upper mantle flow. For
120 instance, the relationship between gravity signals and topography through the analysis of
121 admittance, in addition to the presence of uplifted shorelines, suggest a long-term contribution of
122 the mantle to regional uplift (D'Agostino et al., 2001b). The role of active faulting in river
123 drainage capture suggests a contribution from a broad regional uplift of the lithosphere (Geurts et
124 al., 2018). The presence of residual topography in the central Apennines is consistent with the
125 dynamic support from the uppermost mantle, suggesting upward flow (Faccenna et al., 2014b).
126 Mantle structure is constrained by seismic tomography which reveals a high wave speed
127 anomaly whose depth range and shape suggest the presence of a sinking slab (e.g., Faccenna et
128 al., 2014b; Giacomuzzi et al, 2011). However, issues of image resolution and coverage still exist,
129 making it difficult to determine the scale of mantle circulation, degree of continuity of the slab,
130 and degree to which it is dynamically connected the upper plate.
131
132 Here we use geodetic constraints to show that the uplift of the Apennines extends along the
133 entire length of the chain, increasing long wavelength relief by 1-2 mm/yr. These results are
134 based on a new GPS velocity solution that employs a larger number of stations and is developed
135 using the latest processing models and standards, referred to the IGS14 global reference frame.
136 We show that there is a very close alignment between the area of uplift and active strain rates,
137 seismicity and modern topographic drainage divide. These relations point to an intimate

relationship between active crustal uplift, mantle flow, crustal extension and landscape development of the Apennines, suggesting that they share a common dynamic source.

2. Data

2.1 GPS Data Processing and Filtering

We use GPS data collected from multiple high precision GPS networks that comprise the data holdings of the Osservatorio Nazionale Terremoti (ONT), Instituto Nazionale di Geofisica e Vulcanologia (INGV). The ONT-INGV data come from a set of 1648 stations whose geographic distribution is focused on Italy, but whose total coverage extends from latitude -40˚ to 79˚, and longitude -69˚ to 129˚. The individual networks and links from which we obtained data are listed in Supplementary Table S1. Data from this collection have been processed using the Gipsy software (v. 6.3) from the Jet Propulsion Laboratory (JPL) and associated JPL data products (satellite orbits, clocks, Earth orientation parameters) to solve for daily (24 hour) positions in a daily free-network, satellite-based reference frame. For the ensuing analyses we realized two versions of station time series in the ITRF2014 reference frame (Altamimi et al., 2016). The first realization used the global JPL x-files to transform daily positions in the free-network, satellite-based frame to the ITRF2014 frame. The Helmert parameters in the JPL x-files are derived from a global distribution of stations and are thus unlikely to be affected by hydrological loading at regional scale. Because we are primarily interested with relative horizontal and vertical motions across the Apennines we realized an additional version of the ITRF2014 time series applying a continental-scale, common-mode filtering (Wdowinski et al., 1997) to reduce the impact of daily noise in the network solution. This filtering is realized by calculating the Cartesian coordinates and velocities from the “global” ITRF2014 daily solutions

for 132 stations in and around the Eurasia plate selected by specific quality criteria. This solution is aligned in origin and scale with ITRF2014 but it is implemented to have no-net rotation with respect to the stable interior of the Eurasian plate, by subtracting a rigid rotation estimated from a 32-station core subset. This reference frame realization method transforms the station time series into a plate-fixed frame and effectively applies a continental-scale spatial filter to the station coordinates, leading to a reduction of the common-mode errors (Wdowinski et al., 1997), and to an increase of the signal-to-noise ratio. The first set of time series was used to calculate the effect of hydrological loading and its possible effects on the uplift rate (section 5.1) whereas the second set was used to estimate the horizontal and vertical displacement rates with MIDAS (section 2.2).

2.2 MIDAS Velocities

To estimate rates of motion for each station we applied the robust MIDAS trend estimator (Blewitt et al., 2016) to obtain the three-component modal velocity from the filtered time series. MIDAS is a non-parametric statistical method that estimates the time series trend by computing the median of rates made from all pairs of data with a time difference of about 1 year (Theil, 1950; Sen, 1968). The algorithm is generally, by design, blind to seasonality, outliers, undocumented steps and heteroscadasticity. In blind tests MIDAS has been shown to be very accurate, to produce realistic uncertainties, and also has short computation time and so is efficient to use on large datasets.

2.2.1 Time Series Discontinuities

While MIDAS is generally robust, even in the presence of (even unknown) discontinuities in a time series, it can be used with an option where data pairs crossing times of known potential

184 steps are omitted. This further ensures that the analysis is not impacted by the presence of
185 equipment or earthquake related steps in the time series. We used this option in conjunction with
186 a database of known equipment and earthquake events. The equipment discontinuity event
187 database is generated from IGS site logs and RINEX data headers whose metadata indicate when
188 a receiver or antenna type or model changed. It is publicly available at
189 http://geodesy.unr.edu/NGLStationPages/steps.txt (Blewitt et al., 2018). We consider a potential
190 earthquake-related step when its magnitude has M>5.5, occurred within a station's observation
191 time interval, and was located within an empirically derived distance between event epicenter
192 and station, defined by $10^{(M/2 - 0.8)}$ degrees, where M is magnitude. For many of the events there
193 was no visible offset of the time series, which can happen if the earthquake is near the distance
194 limit or the equipment change was between similar devices. In practice inclusion or omission of
195 these steps has a significant impact on only a very small fraction of station velocities. In our
196 dataset 97%(99%) of the vertical(east) MIDAS velocities change by less than 1 mm/yr when
197 including steps information. This stability is attributable to the limited number and small size of
198 actual discontinuities in the dataset, and to the robustness MIDAS has when solving for trends in
199 the presence of steps. Because the next stage of the imaging analysis described below is itself
200 also robust to velocity noise, considering the step times has almost no impact on the final
201 outcome of the analysis. In what follows we show results for the case where the steps are
202 included.
203
204 **2.2.2 Statistics and Uncertainties**
205 In Figure 2 we show histograms for the subset of stations having location inside the geographic
206 bounds of Figure 1, at least 2.5 years of position time series duration, and MIDAS vertical

velocity uncertainty of less than 2 mm/yr. There are 648 GPS stations meeting these criteria. Stations, networks, locations and velocities are listed by name in Supplemental Table 2. The histograms of time series duration indicate that most of the stations have as much as 19.4 years, with a median of 8.7 years of data. Thus, they are sensitive primarily to deformation that occurred over the last two decades. Time series completeness is skewed heavily towards 100%, with a median completeness of 89.0%. However, some high quality stations with more sparse occupation schedules where included, though only 2.5% (15%) of the stations have completeness less than 50% (75%). The histograms of vertical velocity uncertainty show that the exclusion of stations with uncertainty greater than 2 mm/yr effects a small number of stations, and that the vast majority of horizontal rate uncertainties are less than 0.5 mm/yr.

2.2.3. Correction for Glacial Isostatic Adjustment

Following the Last Glacial Maximum (LGM) the loss of continental ice sheets changed the surface loads of northern Europe, resulting in an ongoing contemporary Earth surface motion in all three components across the Mediterranean (Haskell, 1935; Vening Meinesz, 1937). These movements extend across the Mediterranean and must be accounted for if we wish to focus on surface motion attributable to the more local to regional Apennine tectonics and mantle dynamics. Serpelloni et al., (2013) discussed similarities and differences between the predictions from two recent independent models, ICE5G (VM2) (Peltier, 2004) and the model of Lambeck et al., (1998) in the Mediterranean region. They found that while the models differ slightly in terms of vertical rates and the steepness of their gradients from the European platform north of the Alps to the central Mediterranean, they agree that the signal along the Italian Peninsula is predicted to

229 be subsidence, dipping approximately linearly towards faster subsidence rates between -0.3 and -
230 1.0 mm/yr to the southwest.
231
232 In following sections we discuss the pattern in uplift rate that we find for the Italian Peninsula.
233 The pattern we observe is not similar to the predicted ramp in subsidence from GIA, and thus the
234 GIA process is not a likely explanation for these signals. However, GIA can affect all the
235 stations similarly, and so give the impression of overall subsidence and obscure the signals of
236 active relief generation that increases and decreases elevations near the Apennines. As
237 mentioned above we focus on signals attributable to tectonics and mantle dynamics on Italy so
238 we correct the velocities for GIA by subtracting the predictions of the more recent ICE-6G
239 model (Peltier et al., 2015) interpolated to the GPS stations used in our analysis (Supplementary
240 Figure 1). We acknowledge that the GIA model predictions have their own uncertainties and
241 that residual signals from the GIA process may remain. However, because the ice depocenter
242 was distant to the north, residual GIA signals can be approximated as a gentle ramp across Italy
243 on the order of a few tenths of a mm/yr or less. The ICE-6G model has less rapid Mediterranean
244 subsidence compared to the model of Lambeck et al., (1998), so correcting with the latter model
245 would result in faster uplift than we show below. The median vertical rate of the filtered IGS14
246 rates after correction for the effects of GIA is -0.05 mm/yr, and the median vertical rate in the
247 image is -0.17 mm/yr, which are both statistically indistinguishable from zero. This suggest that
248 the correction removed long wavelength signal that is not related to local tectonic activity.
249

250 # 3. Methods

251 ## 3.1. GPS Imaging

252 To robustly estimate the three-component velocity fields we use GPS Imaging which includes
253 the determination of time series trends using MIDAS (Hammond et al., 2016). The imaging uses
254 a weighted-median strategy which makes it effective for identifying the part of a spatially
255 variable signal that is consistent across multiple stations. The technique estimates field values on
256 a discrete regular grid points using Delaunay triangulation of the GPS network with an ad hoc
257 inclusion of the grid point. Each grid point estimate is based only on the values at neighboring
258 stations within the ad hoc triangulation, which is repeated anew for every point. The geographic
259 resolution of the imaging is limited only by the station spacing. The estimated field is insensitive
260 to outlying data of arbitrary magnitude as long as they are isolated, i.e., not corroborated by
261 neighboring data. Therefore, the stability and appearance of the field is derived from consensus
262 among the data and not from averaging or classical smoothing through any least-squares
263 formalism.
264
265 The medians are weighted by the value of a spatial structure function (SSF) derived from the
266 data, divided by the data uncertainty (Hammond et al., 2016). Our derivation of the SSF is
267 provided in the Supplementary text. In practice the results of the imaging are insensitive to the
268 details of the SSF when the network is dense, but has more impact at grid points where station
269 density is sparse or asymmetric on either side of a grid point. For both vertical and horizontal
270 component imaging we apply a preliminary median spatial filtering of the velocities to remove
271 outliers, and then interpolate with GPS Imaging to obtain a gridded field. We perform the
272 imaging using all velocities from stations located within a latitude/longitude bounded box that
273 superscribes the area of Figure 1 by at least one degree. This prevents undesirable edge effects in
274 the imaging that could occur if we exclude stations immediately outside the model domain.

Finally, to further enhance the robustness of the estimated field, we repeat the imaging 20 times, using a randomly selected 75% of the velocities each time, and for every pixel we take the median value of the images. This step further reduces the ability of individual GPS velocities to impact the result.

3.2. Uncertainty in GPS Imaging

The ability that GPS Imaging has to resolve geographic patterns of uplift and deformation depends on the size of the signals compared to the uncertainties, in addition to the density and location of stations in the GPS network. The velocities at each pixel are constrained by observations at multiple locations and thus have uncertainties less than those at at individual stations. For example, the median vertical velocity uncertainty at the stations derived from MIDAS is 0.65 mm/yr, while the median formal uncertainty of vertical rates estimated at grid points in the images is ~0.28 mm/yr. We assess the ability of GPS Imaging to resolve the rates and patterns of uplift across the Apennines by performing a sequence of tests that take the actual station locations into account (see Supplementary Materials). The results of these test show that the main uplift signal along the length of the Apennines and continuing into Calabria and northern Sicily are consistent in all tested subsets of the data. We tested cases by choosing subsets of time periods, different halves of the stations selected quasi-randomly, and different time series duration cutoff thresholds, all arriving at essentially similar results. The stability of the derived field is attributable to many factors, including extensive GPS network coverage, with improvements in the number, geographic density and redundancy of stations in the network, duration of time series resulting in low rate uncertainties, improvement in GPS data processing, reference frame stability, and additionally the robustness of our imaging methods. We conclude that having a broad and dense distribution of long duration time series (>10 years data) is

298 essential for resolving the signals of geographically coherent vertical uplift in the Apennines (see
299 Supplement). The vertical rate field we obtained is shown in Figure 3.
300

301 # 4. Results

302 ## 4.1. GPS Imaging Apennine Uplift

303 The vertical rate field along the Italian Peninsula indicates upward motion of the entire Apennine
304 chain (Figure 3). Positive uplift extends continuously from the northern Apennines, adjacent to
305 the Po Plain following a zone that extends uninterrupted to the southern tip of Calabria in the
306 south. Across the Strait of Messina the uplift continues into Sicily. Uplift in northeast Sicily is
307 clearly enhanced by time-variable magmatic inflation of Mount Etna (e.g., Bonaccorso et al.,
308 2015) and so is likely not representative of processes effecting the rest of the Apennines.
309 However, the uplift signal exists in GPS stations in western Sicily as well, continuing to west of
310 Palermo, with an uplift rate similar to the rest of the Apennines.
311

312 North of the Apennines, on the Po Plain subsidence clearly dominates the vertical rate field
313 between the northern Apennines and the Alps. This is one of the largest and most robust parts of
314 the signal in the imaging. Station coverage here is strong and the magnitude of the signal is
315 greater than the rate uncertainties and greater than the signal in the Apennines. The median rate
316 of subsidence is near -4 mm/yr but is greatest toward the Adriatic coast and municipality of
317 Venice. This signal has been attributed to processes such as sediment compaction, aquifer
318 depletion, and geodynamic subsidence and so the total uplift is likely attributable to a
319 combination of pumping, geologic, tectonic and mantle driven processes (Bennett et al., 2012;
320 Bock et al., 2012; Carminati et al., 2003; Devoti et al., 2011; Gatto and Carbognin, 1981;

Serpelloni et al., 2013; Tosi et al., 2002). The GPS Imaging result shows a transition between subsidence in the Po Plain and uplift in the Northern Apennines (up to ~1 mm/yr) that very closely follows the topographic transition. Uplift in the Emilia Romagna section of the Northernmost Apennines is subdued, near 0 mm/yr, but is upward relative to the Po Plain to the northeast and to the Ligurian Coast near Pisa and Viareggio to the southwest.

To show details of the Apennine uplift signal we create three 100 km-wide profiles of vertical velocity along the Italian Peninsula drawn normal to the average trend of the Apennine chain (Figure 4). These show that the uplift generally has a peak near the topographic drainage divide. However, the peak in velocity is wide and not limited to the location of the divide. The uplift is a broad doming with wavelength between 100 and 150 km, wide enough to encompass the width of the high Apennine elevations. For reference on the profiles we plot the location of an Early Pleistocene shoreline that has been uplifted to between 220 and 480 meters above sea level (D'Agostino et al., 2001b; Mancini et al., 2007), its location is shown on Figure 1. While uncertainties and disagreement about the age of the shoreline exist (Mancini et al., 2007; Cosentino and Fubelli, 2008), it is likely that the movement started at 2.5 to 1.5 Ma, suggesting an uplift rate in the range 0.1-0.3 mm/yr. Conservatively accounting for uncertainty we plot a bar on Figure 4 that shows a range of uplift rate from 0 to 0.5 mm/yr at the location of the shoreline. Comparison between the GPS measured uplift and this long-term uplift rate indicate agreement to within this level of uncertainty, with the northern profile on the high range and the central profile on the lower range.

343 The flanks of the uplift, near the Tyrrhenian and Adriatic coasts at the SW and NE ends of all the
344 profiles, have rates that are near zero or downward (Figure 4). An embayment of subsidence,
345 with rates between -0.5 and -1.0 mm/yr primarily impacts the NE end of the northern and central
346 profiles between the Apennine crest and the Adriatic coast (Figure 3). This zone lies within the
347 Apennine fold and thrust belt, a structural remnant of convergence associated with west directed
348 subduction of Adriatic lithosphere and Neogene formation of the Apennines (e.g. Kligfield,
349 1979; Elter et al., 2003; Pace et al., 2015; Patacca and Scadone, 1989).
350
351 West of the drainage divide the vertical rate image in Figure 3 shows three equant anomalies that
352 lie near restive volcanic complexes. These systems are Campo Flegrei to the south, the Alban
353 Hills 20 km southeast of Rome, and an area in Tuscany that roughly includes the Monte Amiata
354 and Larderello geothermal fields. All three of these areas display some characteristics of active
355 magmatic systems. The Monte Amiata-Larderello area has an active geothermal field (Gianelli et
356 al., 1997; Batini et al., 2003), the Alban Hills caldera has minor earthquakes and was the location
357 of a major eruption at 36 ka (Cecconi et al., 2010; Freda et al., 2006), and the Campi Flegrei near
358 Naples has experienced large uplift over 10k years and contemporary unrest in the 20th century
359 (Isaia et al., 2009). Uplift signals from the Monte Amiata-Larderello and the Alban Hills
360 anomalies appear on our northern and central GPS profiles, respectively, but the Campi Flegrei
361 anomaly lies too far north of the southern profile and so does not appear (Figure 4). On the SW
362 side of the northern profile the anomaly reaches 1 mm/yr uplift and rises above the anomaly that
363 is centered on the drainage divide to the east. The Alban Hills has a somewhat lower intensity
364 anomaly (< 1 mm/yr) on a second hump on the west side of the central profile. The fact that
365 these anomalies are associated with volcanic systems may indicate that they are not as long lived

366 as the anomalies near the central Apennines that we attribute to tectonic uplift. This may explain
367 why the uplifted Early Pleistocene shorelines in Figure 4AB appear east of the current uplift
368 anomalies. On the other hand the geodetic uplift signal in Tuscany spatially corresponds with
369 the area of uplifted Plio-Quaternary sediments along the Tyrrhenian side of the Apennines
370 (Marinelli et al., 1993) with the main peaks reached at Larderello and Monte Amiata geothermal
371 fields for both the long-term and geodetic signals (Figure 5). This correspondence may suggests
372 that the magmatic intrusions responsible for the Larderello and Monte Amiata geothermal fields
373 (Gianelli et al., 1997; Batini et al., 2003) are still active.
374
375 To the south stations on the Aeolian Islands in the Mediterranean Sea north of Sicily experience
376 downward motion overall, but are also effected by volcanic deformation of e.g., the islands of
377 Volcano, Stromboli, etc. (e.g., Cintorrino et al., 2019). While it is possible with GPS Imaging to
378 interpolate the vertical field into areas covered by the Mediterranean sea, we have chosen to omit
379 from the images all areas covered by the sea since it is generally not well sampled with GPS
380 stations that have not been effected by active volcanic deformation. However, we do include
381 island data in the imaging of onshore vertical land motion. The masking of the sea-covered areas
382 could lead to some bias in the impression given by the inferred uplift pattern. However, as
383 shown above, the Apennine uplift consistently tends to zero on the Tyrrhenian and Adriatic
384 coasts indicating that the vertical rate anomaly is focused on the Apennine crest.
385

386 **4.2. GPS Imaging Horizontal Velocity**

387 Previous studies of horizontal GPS velocities have shown the general pattern and rates of active
388 extension across the Apennine chain (e.g., Bennett et al., 2012; D'Agostino et al., 2001a; 2011;

389 D'Agostino, 2014; Devoti et al., 2011; Serpelloni et al., 2005). We here apply GPS Imaging to
390 the east and north component MIDAS velocities to obtain a gridded version of the velocity field
391 that can be compared to the vertical rate field. For the horizontal imaging we use the same SSF
392 that we derived for the vertical velocities in order to maintain consistency in the signal
393 wavelengths preserved in the imaging. In Figure 6A we present the MIDAS horizontal velocities
394 and in Figure 6B the gridded version obtained with GPS Imaging decimated by a factor of 2
395 from the underlying node density for visual clarity.

396

397 We find, similar to previous studies, ~3 mm/yr of near-uniaxial spreading in a zone of extension
398 that is centered on the Apennine chain. These steepest velocity gradients are focused directly on
399 the drainage divide (Figure 6). This is clearer in the profiles of horizontal magnitude of velocity
400 (Figure 7) that have the same locations as the profiles in Figure 4. These show that the steepest
401 velocity gradient delineates a zone of accommodation that is 25 to 40 km wide and almost
402 always within the range of along-profile distances defined by the drainage divide.

403

404 There is sparse distribution of velocities on the Dalmatian coast and Dinaride Alps east of the
405 Adriatic, but given the greater number of very consistent velocities on the Adriatic coast of Italy,
406 there are enough to allow preliminary reconstruction of the velocity field across the Adriatic.
407 The velocity gradients are gentle and describe a northeast movement with azimuths that vary
408 with latitude up the Adriatic Sea. The changes in gradients may be attributable to lack of rigidity
409 and distinct kinematics between the northern and southern Adriatic (D'Agostino et al., 2008;
410 Oldow et al., 2002).

411

412 **4.3. GPS Imaging of Horizontal Strain Rate**

413 From the gridded horizontal velocity field we estimate the velocity gradients attributable to
414 crustal strain rates. Deriving strain rates from the gridded field improves geographic balance in
415 the strain rate solution and reduces the tendency for the solution to work more heavily to satisfy
416 data where stations are densely spaced. The technique evaluates strain at every grid point in the
417 model, using a Gaussian weighting function to more heavily weight stations that are closer to
418 each evaluation point (Hammond et al., 2019). Choosing an optimal value for the width of the
419 weighting function is non-unique. We select the width w = 8 km, which is chosen because it is
420 low enough so that model misfit is low, and large enough to suppress artifacts (see supplemental
421 materials). We use the relations of Savage et al., (2001) to solve for components of rotation and
422 strain rate on the surface of a sphere. A map of the dilatational strain rate (the sum of the two
423 principal strain rates e_1 and e_2) is shown in Figure 8. In our convention negative values are
424 contraction and positive values are extension (area growth). We focus on the dilatational strain
425 rate because the Apennine deformation zone is in uniaxial extension, a condition where $\dot{e}_1 > 0$
426 and $\dot{e}_2 \approx 0$, so dilatation corresponds to the uniaxial strain rate.
427
428 The map shows a robust stripe of high strain rates (>50 x 10^{-9}/yr) in a zone corresponding to the
429 location of the Apennine drainage divide (Figure 8) and M > 6 earthquakes (Rovida et al. 2019).
430 Similar to the uplift, the strain extends along the entire length of the Apennine chain, from the Po
431 Plain to southern tip of Calabria. Also similar to the uplift, the strain continues across the straight
432 of Messina, passes through the active zone affected by Etna volcano, and continues into northern
433 Sicily. Also, west of the main axis of strain rate there is a secondary stripe of active strain that
434 aligns with the secondary zone of uplift, which is occupied by restive volcanic zones discussed

435 above and shown in Figure 3. The strain is plotted on the profiles (Figure 7) showing that the
436 secondary zone of strain to the west has lower amplitude, and is aligned with the secondary
437 uplift. In the northern and central profiles the western secondary zone of uplift is the greater of
438 the two, but the strain rates are greater near the uplift focused on the Apennine drainage divide.
439 This suggests that the Apennines are the primary locus of uplift and strain, and that the western
440 uplift, corresponding to weaker crustal strain is enhanced by the magmatic systems beneath the
441 scattered volcanic systems of western Italy.
442

443 # 5. Ruling out Transient Processes

444 ## 5.1. Hydrological Loading Effects?

445 Recent geodetic studies of mountain uplift has found that it may in some cases be driven
446 primarily or in part by short term transient hydrological surface loads that vary seasonally (e.g.,
447 Amos et al., 2014; Argus et al., 2014; Chanard et al., 2014; Fu and Freymueller, 2012; Fu et al.,
448 2015; Heki, 2001) or have trends driven by multi-annual to decadal changes in surface water
449 content (Amos et al., 2014; Argus et al., 2017; Chen et al., 2018; Fu and Freymueller, 2012;
450 Hammond et al., 2016) and not necessarily related to long-term development of the topography.
451 A previous study in the Southern Apennines focused on the hydrological contribution to seasonal
452 and multi-annual transient deformations, showing that upward motion averaged by multiple
453 stations is inversely correlated with Equivalent Water Height signal from GRACE (Silverii et al.,
454 2016). This motivates us to consider if a drying and unloading trend, whose temporal scale is
455 longer than the multi-annual signal (4-5 years) observed by Silverii et al. (2016) could explain
456 the observed uplift signals in the Apennines.
457

458 To address this question we consider data from the GRACE satellite mission which measures the
459 Earth's time-variable gravity field, and is sensitive to the changing distribution of surface water
460 which can cause vertical motions via loading. Data from GRACE collected from 2003 to 2016,
461 overlaps the time of collection of our GPS data. We considered the JPL (Watkins et al., 2015;
462 Wiese et al., 2016) and GSFC solutions (Luthcke et al., 2013) accessed via the mascon
463 visualization tool developed by the University of Colorado (https://ccar.colorado.edu/grace/).
464 GRACE spatial resolution is typically on the order of 300-400 km, larger than the width of the
465 Apennines (~200 km). Thus, all GRACE mascons intersect one of the Adriatic, Tyrrhenian or
466 Ionian seas to some degree. As a result the solutions may be partially influenced by the changing
467 gravity owing to Mediterranean Sea level changes, in addition to the terrestrial water storage.
468 These leakage errors are addressed specifically in the JPL solution, where an attempt was made
469 to partition the gravity signal into sea and land components (Watkins et al., 2015). The GSFC
470 mascons are smaller so overlap less with the sea, but may be affected by correlation between
471 adjacent mascons, and associated errors.
472
473 However, while these considerations indicate uncertainties in the GRACE products, we observe
474 that the gravity trends for all the mascons near the Apennines are positive suggesting mass gain
475 over time. We illustrate this for an example equivalent water height (EWH) time series solution
476 for GSFC mascon #5339 that covers Naples and a large part of southern Italy (Figure 9A), which
477 has a trend of 0.41 cm/yr. We compare this to a stack of vertical time series for GPS stations
478 included within the area defined by the mascon #5339 characterized by low scatter, and step-free
479 time series. To avoid suppression of loading signal from our filtering of common-mode signal,
480 for this analysis we used IGS14 position time series obtained directly from the global

481 transformation parameters (x-files) provided by JPL (see section 2.1). The stack of these GPS
482 vertical time series (Figure 9B) has an upward trend of 0.58 mm/yr modulated by seasonal and
483 multi-annual signals whose source is likely hydrological surface loading (Silverii et al., 2016).
484 Aside from their trends the structure of the GRACE and stacked GPS time series in their
485 seasonality and multi-annual patterns are, in fact, similar. This can be seen in by comparing
486 detrended GPS vertical and GRACE time series (Figure 9C). Also we show a scatter plot of the
487 monthly GRACE value (in units of cm EWH) against the monthly median GPS value (in mm
488 vertical position) (inset in Figure 9C). From these data we calculate a regression between the
489 two variables which has a slope of -0.45 mm/cm which can be considered a linear transfer
490 function between the hydrological forcing EWH (input) and the resulting vertical motion
491 (output). Assuming that the observed trend in the stacked GPS time series is exclusively caused
492 by hydrological forcing, this linear transfer function can be used to estimate the predicted EWH
493 trend. In other words we use the observed elastic response of the Earth surface at seasonal and
494 multi-annual scales to predict the EWH trend expected in the hypothesis of hydrological
495 unloading. The resulting predicted EWH trend expected from the GPS data has a negative slope
496 (0.58 mm/yr/-0.45 mm/cm = -1.3 cm/yr blue in Figure 9A) in contrast to the actual GRACE data
497 which has a positive slope. We conclude from this simple test that, while the GPS and GRACE
498 signals have very similar structures, and are likely measuring the same seasonal to multiannual
499 surface water variability, they differ in their trends and thus are measuring different long-term
500 processes.
501
502 This result is representative of other mascons covering the Apennines that show trends of
503 between 1 to 5 mm/yr of increasing EWH over the period of observation (the range considers

differences between, and spatial variation of GSFC and JPL solutions). These trends are near the level of uncertainties, but are consistently positive over the Apennines. Thus, despite the uncertainties and resolution issues involved in the GRACE results, they do not seem to support the occurrence of a drying trend that could explain the uplift. The GPS data seem to have trends that are not predicted by GRACE EWH estimates and thus likely have a different origin.

One possible interpretation of these observations is that increasing terrestrial water storage explains the GRACE data, but is not sufficient to provide enough loading to overcome mantle flow driven Apennine uplift. However, another possibility is that the GRACE signal is in whole, or in part, caused by an increase in mass associated with the uplift rather than surface hydrology. A mass increase would be observed, for example, if vertical mantle flow-related uplift was accompanied by horizontal mantle flowing inward to the asthenosphere beneath the Apennines, this would imply an increase in the length of the vertical mantle column to support the rising elevation. Moreover, owing to the greater density of mantle rocks compared to water, uplift from mantle flow will be over 3 times as effective in creating an EWH signal. Below we discuss our estimate of vertical mantle flow that is near 2 mm/yr, which is consistent with GRACE trends we observe of 0.4 cm/yr trend in EWH (Figure 9A). In this interpretation the mass gain seen by GRACE is not attributable to water, but to the increase in the amount of mantle rock mass beneath the satellite.

5.2. GPS Velocity Variability

In the discussion that follows we attribute the uplift imaged in Figure 3 to processes at work in the lithosphere and upper mantle. The scale of these processes suggest that, like plate tectonics,

527 they proceed steadily over the periods of time we observe with GPS. We do not expect that
528 uplift derived from mantle flow will vary substantially over a few years time. Thus the time
529 variability of GPS velocity is one characteristic that can indicate when GPS data are not
530 representative of movements associated with geodynamic processes that persist over long
531 periods, possibly millions of years.
532
533 To assess the time variability of the uplift field we compute for each vertical GPS time series an
534 index based on the MIDAS algorithm (Blewitt et al, 2016). For each time series we take 2-year
535 long sub-intervals and compute the MIDAS rate for each interval. We start with the first 2 years
536 of the time series, then select a new interval by shifting the window forward in time by one
537 month, and repeat the process until the window extends beyond the end of the time series. The 2-
538 year window size is selected because it is long enough to include enough data pairs separated by
539 one year to compute the MIDAS rate, yet short enough so that many rate samples can be
540 generated for the time series in our dataset. The result is a time series of MIDAS velocity for the
541 station which indicates how the rate changed over the period of observation. This variability
542 index is insensitive to outliers and seasonal periodicity because MIDAS rates are computed from
543 pairs of data separated by one-year duration. Hence the index represents a robust measure of
544 *non-seasonal variability* (NSV) in velocity. To compute the index we take the median absolute
545 deviation (MAD) of the values in the velocity time series:
546
547 $$V_{u,NSV} = MAD(V_{MIDAS}([t_i - 1.0, t_i + 1.0])) \quad (1)$$
548

549 which has units of mm/yr. Here V_{MIDAS} is the MIDAS velocity obtained from the interval of
550 vertical component time series data over the 2 year interval [t_i - 1.0, t_i + 1.0] which is centered
551 on t_i. Using the MAD (as opposed to the standard deviation) in (1) adds an additional layer of
552 robustness since it is less sensitive to outlier rates that could be present in the velocity time
553 series. Stations with complicated vertical motion history will have larger $V_{u,NSV}$, while stations
554 with very linear trends have low $V_{u,NSV}$. A histogram of $V_{u,NSV}$ indicates the center, body and
555 range in the distribution of $V_{u,NSV}$ values, 75% of which are less than 1.8 mm/yr (Figure 10A). A
556 histogram of $V_{u,NSV}$ normalized by the uncertainty of the MIDAS rate for the full time series
557 (Figure 10B) indicates that 34% of have $V_{u,NSV}/\sigma_{Vu}$ values greater than 2, suggesting that for
558 this minority of stations the time variability is significant.
559
560 To test whether any important signals in uplift map in Figure 3 could be driven by time-variable
561 uplift processes we repeat the imaging using only vertical rates from GPS stations that have V_{NSV}
562 less than the median variability (1.8 mm/yr). This is similar to the other tests of robustness in
563 which we repeated the imaging while omitting half the data, as presented in the supplemental
564 materials. The result (Figure 10C) shows that the imaged uplift rate is very similar to the image
565 made using all of the data, with the same major domains and rates of uplift and subsidence.
566 While individual stations can have high values of $V_{u,NSV}$, those stations tend to be isolated and
567 their impact is reduced by the robust imaging. Thus, the pattern of vertical land motion is
568 supported by the least time-variable rate data.
569
570 **5.3. Earthquake Cycle Effects?**

571 The Apennines are one of the most productive earthquake regions in Italy and home of some of
572 the largest and most damaging events. Maps of earthquake epicenters (Rovida et al., 2019) and
573 hazard (Stucchi et al., 2011) show a strong correlation to the zone of uplift, but this is because
574 the uplift is correlated with the active plate boundary deformation, not because the earthquakes
575 or their aftershocks, or subsequent postseismic deformation, directly causes uplift of Earth
576 surface. However, it has been shown that in extensional tectonic environments large earthquakes
577 (e.g., M7 and above) can exhibit post-seismic viscoelastic uplift or strain that can last for decades
578 (e.g., Gourmelen and Amelung, 2005; Reilinger, 1986). This deformation decays over time at a
579 rate that depends on the elastic and viscoelastic properties of the crust and mantle, and on the
580 postseismic process at play. Thus it may be reasonable to consider the question of whether the
581 observed uplift could reflect a cumulative plate boundary-scale postseismic deformation having
582 contributions from the many normal faults in the Apennines (Riguzzi et al., 2013).
583
584 We argue that this is unlikely. One argument is that the main signal generated by recent
585 Apennine earthquakes is postseismic subsidence rather than uplift. For example, subsidence was
586 observed for the L'Aquila event in 2009 (Albano et al., 2015; Cheloni et al., 2014; D'Agostino et
587 al., 2012) and for the similar Norcia sequence in 2016 (Cheloni et al., 2017). Second, even if
588 postseismic uplift occurs, e.g., as has been observed for multiple large extensional events in the
589 Basin and Range (Gourmelen and Amelung, 2005; Reilinger, 1986), it is statistically improbable
590 that postseismic uplift would be currently present along the entire Apennine chain. If, for
591 example, measurable postseismic vertical motion is detectible over the fault for 100 years after
592 the event, and recurrence intervals are ~2000 years (Galli et al., 2008), each fault would only
593 exhibit postseismic uplift about 5% of the time. In reality recurrence intervals could be much

longer, e.g., Galandini and Galli, (2003) found recurrence intervals of 4690 and 7570 years for the Mt. Vettore Fault and Laga Mtn. Fault respectively. Also, relaxation times may be much shorter, e.g., early constraints on the L'Aquila earthquake in 2009 estimated a relaxation time of ~1 month (Devoti et al., 2012). Thus, it is very unlikely that we would be observing postseismic uplift for more than one Apennine fault system simultaneously, or that the overall uplift pattern we observe is attributable to transient earthquake cycle deformation.

5.4. Long-Term Uplift?

The arguments above suggest that the uplift features we detect in the GPS data are not attributable to transient processes we have considered, or even ones we have not considered if they operate over the duration of GPS observation. The uplift signal may therefore represent a motion that persists for longer periods of time, possibly over an interval that is geologically relevant. This is supported by the comparison between the geodetically measured uplift and the elevation of uplifted shorelines (Figure 4), and the contours of elevation of Neogene sediments (Figure 5). While comparisons of this nature depend on GPS reference frame realization, alignment, sea level changes, and correction for GIA described in Section 2.2.3, the agreement suggests that the GPS uplift field may be related to formation of the topography of the Apennines. The correlation between the uplift and the active crustal extension further suggests that we are seeing a part of the main geodynamic signal controlling active deformation at the scale of the plate boundary.

6. Discussion

6.1. Vertical Mantle Flow Under the Apennines

Previous work has concluded that support for the residual long wavelength topographic bulge across the Apennines from the mantle (D'Agostino and McKenzie, 1999) helps control the locus of extension generating short wavelength topography (D'Agostino et al., 2001b; D'Agostino et al., 2014; Cowie et al., 2017), and that active continuing uplift measured with geodesy is related to that support (Faccenna et al., 2014b). These indicate that the process (or processes) which generate support continue to the present day, and suggest that mantle does not merely statically support topography, and continues to move upward in a flow that increases support over time. However, it is less clear to what extent surface geodetic observations directly reflect vertical flow of the asthenosphere. We explore this question in the next section by asking: How fast is the vertical flow of the mantle beneath the lithosphere that drives the surface upward?

If the lithosphere is a static plate being displaced upward from its base we might expect the surface to move upward at the same rate. However, the Apennines do not merely rise, they also deform under approximately uniaxial extension as we have seen in our GPS results (Figure 8). When the lithosphere experiences horizontal dilatational strain it is expected to thin and subside (McKenzie, 1978), yet we observe uplift (Figure 3). Thus, the bottom of the lithosphere must be moving upward more rapidly than the observed surface motion to compensate for the stretching-related thinning. We estimate the vertical rate at the bottom of the lithosphere by adding the surface uplift rate expected from the horizontal stretching. We use a relationship based on a model of isostatic compensation of a stretching lithosphere/crust system (McKenzie, 1978) subject to heat flow, but no elastic thickness, that can support a long-term load (from Howell et al, 2017):

$$\dot{S}_i \approx \frac{t_l[(\rho_0-\rho_c)\frac{t_c}{t_l}(1-\alpha T_1\frac{t_c}{2t_l})-\frac{\alpha T_1\rho_0}{2}]}{\rho_0(1-\alpha T_1)-\rho_w}(\dot{e}_1+\dot{e}_2) \qquad (2)$$

640

641 $$\dot{S}_i \approx f_i(\dot{e}_1 + \dot{e}_2) \quad (3)$$

642 Here $\dot{S}_i$ is the surface subsidence rate (positive downward), $\dot{e}_1 + \dot{e}_2$ is the surface horizontal
643 dilatational strain rate. We assume that densities at 0°C for mantle ρ_0 and crust ρ_c to be 3300
644 and 2700 kg m^{-3} respectively and for water ρ_w to be 1000 kg m^{-3}. The factor f_i in equation (3)
645 is a term containing the physical parameters in equation (2) and scales the dilatational strain rate
646 to estimate the subsidence rate. Following McKenzie et al., (2005) we adopt thermal expansivity
647 α=3×10^{-5} K^{-1} and test three different values for temperature of the asthenosphere T_1 = 1215°,
648 1315°, and 1415° C. We then calculate f_i for an array of possible lithosphere t_l and crustal t_c
649 thicknesses and plot contours of f_i (Figure 11). This shows that the sensitivity of f_i to
650 temperature and lithospheric thickness is relatively small, while sensitivity to crustal thickness is
651 larger.

652

653 Since f_i is less sensitive to t_l than to t_c, we fix t_l = 55 km, and test thicknesses for the crust of t_c
654 = 35, 45 or 55 km. Crustal thickness estimated from teleseismic receiver functions is 40-45 km
655 (Piana Agostinetti & Amato, 2009), so we test the others as approximate lower and upper
656 bounds. These parameters result in f_i values of 7900, 10600, and 13300 respectively. These
657 values do not consider thickness of an elastic lithosphere that might reduce the deflection
658 associated with extension, and so are upper bounds. This analysis also ignores the possible
659 contribution of magmatic additions to the lithosphere upon stretching and decompression melting
660 from ascending mantle rocks. As discussed above, Italy has volcanic activity, but is not a
661 volcanically dominated landscape like, e.g., a mid-ocean ridge environment, so we ignore this
662 possible contribution. Also, this model does not account for short wavelength vertical rate

663 variations that may be expected to occur across locked normal fault systems in their interseismic
664 strain accumulation phase, and should only be compared to the long wavelength vertical rate
665 patterns (i.e., gray bands in Figure 4).
666
667 We illustrate the effect from stretching on the vertical rate field in the profiles of velocity with
668 the estimated contribution subtracted from the vertical rate field (Figure 12). The profiles of
669 predicted subsidence (where positive subsidence has a negative vertical rate) are shown with the
670 smoothed envelopes of GPS measured uplift (from Figure 4). The dashed lines represent the
671 GPS uplift and the gray band indicates the range of possible upward vertical rates (corrected for
672 extensional-related subsidence). It can also be considered as the vertical component of mantle
673 flow beneath the lithosphere given the assumption outlined above. The width of the gray band is
674 wider since the maximum and minimum addition from the stretching model is added to the upper
675 and lower bound uplift profiles respectively, to reflect the total range of possibilities. The
676 enhancement is greatest where the extensional strain rates are highest.
677
678 The vertical motion profiles shown in Figure 12 have fastest rates near the Apennine crest. The
679 northern profile, which prior to enhancement had higher observed uplift west of the crest (near
680 the volcanic fields west of the Apennines) now has similar uplift near the topographic crest of ~1
681 mm/yr. Relief generation across the profile is 1.5 - 2.0 mm/yr. The central profile has uplift
682 over twice the rate it had prior to enhancement, reaching 0.6 mm/yr, whereas relief generation is
683 1.0 - 1.5 mm/yr. The southern profile maximum uplift rate exceeds 1 mm/yr, with relieve
684 generation of 1.5 - 1.8 mm/yr. The higher amount of enhancement on the west end of the
685 southern profile comes from strain associated with Campi Flegrei volcanic system which bleeds

686 into the profile area from the north and is not expected to represent subsidence from plate
687 boundary crustal stretching. Owing to its derivation from crustal strain, the vertical rate of
688 upward mantle flow has a greater degree of alignment between plate boundary strain rate and
689 uplift signals.
690
691 While it is currently not possible to directly observe the vertical motion of the bottom of the
692 lithosphere with geodetic means, the estimates shown in Figure 12 may serve as a proxy for that
693 motion. These results may be of use to those who model chemical and physical evolution of
694 petrological systems or melt genesis during the ascent of mantle rocks.
695
696 **6.2. Scale of mantle flow, subducting slab and slab windows**
697 Previous work has suggested that a slab remnant from the period of Neogene Adriatic subduction
698 is sinking in the upper mantle beneath the Apennines. Evidence for this slab exists in seismic
699 imaging (e.g., Giacomuzzi et al., 2011; Piromallo and Morelli, 2003; Spakman et al., 1993; Zhu
700 et al., 2012, and see Faccenna et al. 2014a for a comparison between models). This slab and its
701 lateral segmentation may play a role in driving vertical mantle flow and to have played a role in
702 coordinating surface tectonics and dynamic elevation and uplift (Bennett et al., 2012; Faccenna
703 et al., 2014b; Shaw and Pysklywec, 2007; Wortel and Spakman, 2000). Geodynamic models
704 suggest that the sign of vertical motion expected from a descending high-density slab depends on
705 several factors including e.g., the degree of detachment and rollback of the slab from the
706 overriding lithosphere, viscosity and density structure (Giunchi et al., 1996). Based on early
707 GPS measurement of uplift that seemed to be limited to the central Apennines, and seismic
708 tomography that showed discontinuous high seismic wave speed anomalies in the uppermost

709 mantle, Faccenna et al., (2014b) concluded that the slab was partially detached, which drove
710 uplift to occur in a limited section of the Apennines.
711
712 Seismic tomographic models that image wave speed anomalies have limited resolution in Italy.
713 Models show differing degrees of continuity of high waves speed anomalies, which can appear
714 continuous or discontinuous in the mantle beneath the trend of the Apennines, depending on the
715 model and depth range considered. In any case, based on these images it is difficult to confirm
716 the degree of completeness of the dynamic connection between the sinking slab and the upper
717 plate from these images. In at least one model the high wave speed anomaly follows closely our
718 imaged uplift zone, even extending south through the Calabrian Arc into the mantle beneath
719 Sicily (Giacomuzzi et al., 2011). However, even in this model the anomalies are discontinuous
720 at 70 km depth, but continuous at 140 km depth.
721
722 In our geodetic imaging of surface motion we observe uplift along the entire length of the
723 Apennine chain, which in light of the arguments presented above would suggest that detachment
724 of the slab from the upper plate is complete. If this is the case it suggests that replacement of
725 high-density sinking slab material with low density asthenospheric mantle is ongoing and its
726 affects are seen by the GPS networks in Italy. It also suggests that because the uplift follows the
727 boundary between Adriatic and Tyrrhenian lithosphere very closely, that uplift, strain, Adriatic
728 microplate translation, and upper mantle flow are all part of a single active and ongoing process
729 that drives contemporary seismic hazard of the Italian Peninsula.
730
731

732 **6.3. Flexural Uplift?**

733 Buoyancy of mantle rocks may not be the only possible source of stresses available to drive
734 upward movement of the lithosphere beneath the Apennines. Another possible source is elastic
735 stresses in the extensional axis flanks that drive uplift when thinning of the extending crust
736 unloads the plate. This process, known as of footwall unloading or ridge-flank uplift, results in
737 rift shoulders and tilting that can be evident in topographic or structural profiles parallel to the
738 extension direction. The model has been used to explain observations in the East African Rift
739 (Vening Meinesz, 1950), Rhine Graben (Weissel and Karner, 1989), Sierra Nevada Mountains
740 (Thompson and Parsons, 2010); Baja California (Mueller et al., 2009), Transantarctic Mountains
741 in Antarctica (Stern and Ten Brink, 1989), and others. This model is important to consider
742 because it explains uplift as a process driven primarily by extension, and does not require vertical
743 flow of material in the asthenosphere. Similar to Baja, California, the Apennines have uplifted
744 shorelines far from the axis of uplift (D'Agostino et al., 2001b; Mueller et al., 2009). However,
745 previous analysis of the admittance between gravity and topography has found that the effective
746 elastic thickness of Italy is thin, roughly 3-4 km (D'Agostino and McKenzie, 1999). Thus, the
747 expected horizontal wavelength and curvature of the response to flexure in the Apennines will be
748 narrower than the wide arc of uplift observed in the topography and our geodetic uplift rates
749 (which is between 100 - 150 km in width). Moreover, the Apennines do not exhibit substantially
750 thinner lithosphere that is ostensibly required for unloading of the flanks. These arguments
751 together suggest that it is unlikely that thinning-related unloading alone can explain the observed
752 uplift signal.
753

754 However, plate flexure may arise from a source unrelated to thinning and unloading. If
755 asthenospheric flow generates uplift by applying pressure to the base of the plate, then flexure
756 would be a response to the plate bending with the variation in uplift rate across the axis. In this
757 case the flexural stress pattern will be a function of the curvature of the uplift profile and the
758 flexural rigidity, a property related to the thickness of the plate and its elastic properties (Turcotte
759 and Schubert, 2002). If we assume that lithospheric properties are constant we can relate the rate
760 of curving, i.e., the second derivative of uplift rate with respect to distance across axis in the
761 envelopes of uplift (Figure 12), to the rate of flexural bending. In Figure 13 we show the mean
762 of the lower and upper envelopes of filtered uplift rate curvature, calculated from the second
763 derivative of the upper and lower edges of the uplift envelope using double finite difference. In
764 this smoothed version of the curvature we see a pattern, consistent across the north, central and
765 southern profiles, where the greatest rate of flexural bending is not on the flanks but centered on
766 the highest topography and drainage divide of the Apennines. Thus, while the Apennine
767 lithosphere is already under extension from plate boundary divergence (Figure 8), it is also at a
768 local maximum of the flexural extension imparted by uplift that varies across the Apennines.
769 This effect may serve to further focus extension at the locus of maximum uplift.
770
771 Multiple mechanisms may be at work to drive the active Apennine uplift, and more detailed
772 mechanical modeling of these effects are likely needed to quantify the relative importance of
773 each contribution. However, the alignment of the separate indicators of crustal deformation,
774 uplift, topography and drainage together suggest that vertical flow-driven flexure can plausibly
775 contribute to the focusing of active seismicity and seismic hazard along the Apennine chain.
776

7. Conclusions

We have presented a new compilation and analysis of GPS data for Italy and its surrounding areas, and we use GPS Imaging technique to show that the relief of the Apennines Mountain chain in Italy is currently increasing along its entire length by 1 to 2 mm/yr. Relief is increasing in a 100-150 km wide zone with a profile similar to the long wavelength topography, but not similar to the shorter wavelength topography generated by active faulting and erosion. The maximum uplift rates are geographically aligned with the highest elevations, the topographic drainage divide, the location of the highest strain rates associated with extension in the Adriatic/Tyrrhenian plate boundary, and with the areas with fastest uplift rate curvature.

Tests of the variability of the GPS-measured uplift rate, GRACE satellite mission data, and correlation of the uplift with other data pertaining to long-term uplift suggest that it is a long-lived feature.

Uplift occurs despite that the expected consequence of extension is crustal thinning and subsidence. This is consistent with the presence of asthenospheric upward mantle flow of up to 2 mm/yr, possibly associated with buoyant mantle flowing into the space above a sinking slab that is dynamically detached from the upper plate.

These results also suggest that the gravitational forces responsible for the correlation between regional high elevation and active extension in the Apennines, have been excited in the last 2-3 My by the same process that is imaged by the dense GPS network in the Apennines. Spatial scales and amplitudes of vertical motion geodetically observed in the Apennines are consistent

800 with multiscale mantle convection processes inducing dynamic topography at a wide range of
801 scales (Arnould et al., 2018; Hoggard et al., 2016; Kreemer et al., 2020). Continental scale GPS
802 imaging of vertical land motion can provide additional constraints available for studies targeting
803 the topographic expression of mantle flow.
804
805 **Acknowledgements**
806 We thank the operators and data archiving facilities of the 26 high-precision GPS networks in
807 and around Italy that we used for this study, the internet locations from which data were accessed
808 are listed individually in Supplemental Table 1. We obtained GRACE time series data via the
809 University of Colorado Mascon Visualization Tool (https://ccar.colorado.edu/grace/index.html).
810 WCH received support from NASA Solid Earth via projects NSSC17K0565, NNH16ZDA001N,
811 and 80NSSC19K1044 from the University of Nevada, Reno for his sabbatical leave and for
812 travel support via the International Activities grant program. Some figures were made using the
813 Generic Mapping Tools v5.4.1 software (Wessel et al., 2013). WCH acknowledges support from
814 INGV who hosted his visit in Rome.
815

References

Albano, M., Barba, S., Saroli, M., Moro, M., Malvarosa, F., Costantini, M., Bignami, C., & Stramondo, S. (2015). Gravity-driven postseismic deformation following the Mw 6.3 2009 L'Aquila (Italy) earthquake. *Scientific Reports, 5*, 16558, https://doi.org/10.1038/srep16558.

Altamimi, Z., Rebischung, P., Métivier, L., & Collilieux, X. (2016). ITRF2014: A new release of the International Terrestrial Reference Frame modeling nonlinear station motions. *J. Geophys. Res. - Solid Earth,* 121, 6109-6131, https://doi.org/10.1002/2016JB013098.

Amos, C. B., Audet, P., Hammond, W. C., Bürgmann, R., Johanson, I. A., & Blewitt, G. (2014). Uplift and seismicity driven by groundwater depletion in central California. *Nature*, *509*(7501), 483–486. https://doi.org/10.1038/nature13275.

Argus, D. F., Fu, Y., & Landerer, F. W. (2014). Seasonal variation in total water storage in California inferred from GPS observations of vertical land motion. *Geophys. Res. Lett., 41*, 1971–1980, https://doi.org/10.1002/2014GL059570.

Argus, D. F., Landerer, F. W., Wiese, D. N., Martens, H. R., Fu, Y., Famiglietti, J. S., & Watkins, M. M. (2017). Sustained water loss in California's mountain ranges during severe drought from 2012 to 2015 inferred from GPS. *J. Geophys. Res.- Solid Earth, 122*, 10,559–10,585. https://doi.org/10.1002/ 2017JB014424.

Arnould, M., Coltice, N., Flament, N., Seigneur, V., & Müller, R. D. (2018). On the scales of dynamic topography in whole-mantle convection models. *Geochemistry, Geophysics, Geosystems*, *19(*9) 3140-3163, https://doi.org/10.1029/2018GC007516.

Bartolini, C., D'Agostino, N., & Dramis, F., (2003). Topography, exhumation, and drainage network evolution of the Apennines. *Episodes*, *26*(3), 212-216, https://doi.org/10.18814/epiiugs/2003/v26i3/010.

Batini F., Brogi, A, Lazzarotto A., Liotta, D., & Pandeli, E. (2003). Geological features of Larderello Travale and Mt. Amiata geothermal areas (southern Tuscany, Italy). *Episodes 26(3),* p. 239-244, https://doi.org/10.18814/epiiugs/2003/v26i3/015.

Bennett, R. A., Serpelloni, E., Hreinsdóttir, S., Brandon, M. T., Buble, G., Basic, T., Casale, G., Cavaliere, A., Anzidei, M., Marjonovic, M., Minelli, G., Molli, G., & Montanari, A. (2012). Syn-convergent extension observed using the RETREAT GPS network, northern Apennines, Italy. *J. Geophys. Res., 117*, B4, https://doi.org/10.1029/2011JB008744.

Blewitt, G., Kreemer, C., Hammond, W.C., & Gazeaux, J. (2016). MIDAS Robust Trend Estimator for Accurate GPS Station Velocities Without Step Detection. *J. Geophys. Res. - Solid Earth*, 121(30, 2054-2068, https://doi.org/10.1002/2015JB012552.

Blewitt, G., Hammond, W.C., & Kreemer, C. (2018). Harnessing the GPS data explosion for interdisciplinary science, *Eos, 99*, https://doi.org/10.1029/2018EO104623.

Bock, Y., Wdowinski, S., Ferretti, A., Novali, F., & Fumagalli, A. (2012). Recent subsidence of the Venice Lagoon from continuous GPS and interferometric synthetic aperture radar, *Geochem. Geophys. Geosyst., 13*, Q03023, https://doi.org/10.1029/2011GC003976.

Bonaccorso, A., Bonforte, A. & Gambino, S. (2015). Twenty-five years of continuous borehole tilt and vertical displacement data at Mount Etna: Insights on long-term volcanic dynamics. *Geophys. Res. Lett., 42,* 10,222–10,229, https://doi.org/10.1002/2015GL066517.

Carminati, E., Doglioni, C., & Scrocca, D. (2003). Apennines subduction-related subsidence of Venice (Italy). *Geophys. Res. Lett., 30*(13), 1717, https://doi.org/10.1029/2003GL017001.

Cecconi, M., Scarapazzi, M. Viggiani, G.M. B. (2010). On the geology and the geotechnical properties of pyroclastic flow deposits of the Colli Albani. *Bull. Eng. Geol. Env.*, *69*(2): 185–206, https://doi.org/10.1007/s10064-009-0250-x.

Cenni, N., Viti, M., Baldi, P., Mantovani, E., Bacchetti, M., Vannucchi, A., (2013). Present vertical movements in Central and Northern Italy from GPS data: Possible role of natural and anthropogenic causes. *J. Geodynamics, 71* (2013) 74–85, https://doi.org/10.1016/j.jog.2013.07.004.

Cheloni, D., + 12 authors (2014). Coseismic and post-seismic slip of the 2009 L'Aquila (central Italy) M_W 6.3 earthquake and implications for seismic potential along the Campotosto fault from joint inversion of high-precision levelling, InSAR and GPS data. *Tectonophysics 622*, 168–185, https://doi.org/10.1016/j.tecto.2014.03.009.

Cheloni, D., + 41 authors (2017). Geodetic model of the 2016 Central Italy earthquake sequence inferred from InSAR and GPS data. *Geophys. Res. Lett., 44*, 6778–6787, https://doi.org/10.1002/2017GL073580.

Chen, W., Braitenburg, C., & Serpelloni, E. (2018). Interference of tectonic signals in subsurface hydrologic monitoring through gravity and GPS due to mountain building. *Global and Planetary Change, 167*, p 148-159, https://doi.org/10.1016/j.gloplacha.2018.05.003.

Chanard, K., Avouac, J. P., Ramillien, G. & Genrich, J. (2014). Modeling deformation induced by seasonal variations of continental water in the Himalaya region: Sensitivity to Earth elastic structure. *J. Geophys. Res. - Solid Earth, 119,* 5097–5113, https://doi.org/10.1002/2013JB010451.

Cinque, A., Patacca, A., Scandone, P., & Tozzi, M. (1993). Quaternary kinematic evolution of the Southern Apennines, Relationships between surface geological features and deep lithospheric structures. *Ann. Geofis., 36*, 249–260.

Cintorrino A. A., Palano, M., Viccaro, M. (2019). Magmatic and tectonic sources at Vulcano (Aeolian Islands, Southern Italy): A geodetic model based on two decades of GPS observations. *J. Volcan. Geothermal Res., 388,* https://doi.org/10.1016/j.jvolgeores.2019.106689.

Cosentino, D. & Fubelli, G. (2008). Comment on: "Geomorphological, paleontological and $^{87}Sr/^{86}Sr$ isotope analyses on early Pleistocene paleoshorelines to define the uplift of Central Apennines (Italy)." *Quaternary Research, 69*, 163–164, https://doi.org/10.1016/j.yqres.2007.07.014.

Cosentino, D., Asti, R., Nocentini, M., Gliozzi, E., Kotsakis, T., Mattei, M., Esu, D., Spadi, M., Tallini, M., Cifelli, F., & Pennacchioni, M., (2017). New insights into the onset and evolution of the central Apennine extensional intermontane basins based on the tectonically active L'Aquila Basin (central Italy). *Geol. Soc. Am. Bull. 129* (9–10), 1314–1336.

D'Agostino, N. & McKenzie, D. (1999). Convective support of long-wavelength topography in the Apennines (Italy). *Terra Nova, 11*, 234-238, https://doi.org/10.1046/j.1365-3121.1999.00252.x.

D'Agostino, N., Giuliani, R. Mattone, M., & Bonci, L. (2001a). Active crustal extension in the central Apennines (Italy) inferred from GPS measurements in the interval 1994-1999. *Geophys. Res. Lett., 28*, 2121-2124, https://doi.org/10.1029/2000GL012462.

D'Agostino, N., Jackson, J.A., Dramis, F., & Funiciello, F. (2001b). Interactions between mantle upwelling, drainage evolution and active normal faulting: an example from the central Apennines (Italy). *Geophys. J. Int.,* 147, 475–497, https://doi.org/10.1046/j.1365-246X.2001.00539.x.

D'Agostino, N., Avallone, A., Cheloni, D., D'Anastasio, E., Mantenuto, S., & Selvaggi, G. (2008). Active tectonics of the Adriatic region from GPS and earthquake slip vectors, *J. Geophys. Res. - Solid Earth*, *113*, B12413, https://doi.org/10.1029/2008JB005860.

D'Agostino, N., Mantenuto, S., D'Anastasio, E., Giuliani, R., Mattone, M., Calcaterra, S., Gambino, P., & Bonci, L. (2011). Evidence for localized active extension in the central Apennines (Italy) from global positioning system observations. *Geology*, *v. 39*, n. 4, p. 291–294, https://doi.org/10.1130/G31796.1.

D'Agostino, N., Cheloni, D., Fornaro, G., Giuliani, R., & Reale, D. (2012). Space-time distribution of afterslip following the 2009 L'Aquila earthquake. *J. Geophys. Res., 117,* B02402, https://doi.org/10.1029/2011JB008523.

D'Agostino, N., England, P., Hunstad, I., & Selvaggi, G. (2014). Gravitational potential energy and active deformation in the Apennines. *Earth Planet. Sci. Lett., v. 397*, p. 121-132, https://doi.org/10.1016/j.epsl.2014.04.013.

D'Agostino, N., Silverii, F., Amoroso, O., Convertito, V., Fiorillo, F., Ventafridda, G., & Zollo, A. (2018). Crustal deformation and seismicity modulated by groundwater recharge of karst aquifers. *Geophys. Res. Lett, 45* (22), p. 12,253-12,262, https://doi.org/10.1029/2018GL079794.

D'Anastasio, E., De Martini, P. M., Selvaggi, G., Pantosti, D., Marchioni, A., & Maseroli, R. (2006). Short-term vertical velocity field in the Apennines (Italy) revealed by geodetic levelling data. *Tectonophysics, 418*(3–4), 219–234, https://doi.org/10.1016/j.tecto.2006.02.008.

Devoti. R., Esposito, A., Pietrantonio, G., Pisani, A. R., Riguzzi, F. (2011), Evidence of large scale deformation patterns from GPS data in the Italian subduction boundary. *Earth Planet. Sci. Lett., 311*, 230–241, https://doi.org/10.1016/j.epsl.2011.09.034.

Devoti, R., Anderlini, L., Anzidei, M., Esposito, A., Galvani, A., Pietrantonio, G., Pisani A., Riguzzi, F., Sepe, V., & Serpelloni, E. (2012). The coseismic and postseismic deformation of the L'Aquila, 2009 earthquake from repeated GPS measurements. *Ital. J. Geosci. v 131*, n. 3 (2012), 348-358, https://doi.org/10.3301/IJG.2012.15.

Elter, P., Grasso, M., Parotto, M., & Vezzani, L., (2003). Structural setting of the Alpine-Maghrebian thrust belt. *Episodes, v. 26*, n. 3, p. 205–211, https://doi.org/10.18814/epiiugs/2003/v26i3/009.

Faccenna, C., Becker, T. W., Auer, L., Billi, A., Boschi, L., Brun, J.P., Capitanio, F. A., Funiciello, F., Horvàth, F., Jolivet, L., Piromallo, C., Royden, L., Rossetti, F., & Serpelloni, E. (2014a), Mantle dynamics in the Mediterranean. *Rev. Geophys.*, 52(3), 283-332, https://doi.org/10.1002/2013RG000444.

Faccenna, C., Becker, T. W., Miller, M. S., Serpelloni, E., & Willett, S. D. (2014b). Isostasy, dynamic topography, and the elevation of the Apennines of Italy. *Earth Planet. Sci. Lett.*, 407 163–174, https://dx.doi.org/10.1016/j.epsl.2014.09.027.

Freda, C, Gaeta, M., Karner, D.B., Marra, F., Renne, P. R., Taddeucci, J., Scarlato, P., Christensen, J.N, & Dallai, L. (2006). Eruptive history and petrologic evolution of the Albano multiple maar (Alban Hills, Central Italy). *Bull. Volc., 68*: 567–591, https://doi.org/10.1007/s00445-005-0033-6.

Fu, Y., & Freymueller, J. T. (2012). Seasonal and long-term vertical deformation in the Nepal Himalaya constrained by GPS and GRACE measurements. *J. Geophys. Res., 117*, B03407, https://doi.org/10.1029/2011JB008925.

Fu, Y., Argus, D. F. & Landerer, F. W. (2015). GPS as an independent measurement to estimate terrestrial water storage variations in Washington and Oregon. *J. Geophys. Res. - Solid Earth, 120*, 552–566, https://doi.org/10.1002/2014JB011415.

Galli, P., Galadini., F., Pantosti, D., (2008). Twenty years of paleoseismology in Italy, *Earth-Science Reviews, 88*, 89–117. https://doi.org/10.1016/j.earscirev.2008.01.001.

Galandini, F., & Galli, P. (2003). Paleoseismology of silent faults in the Central Apennines (Italy): the Mt. Vettore and Laga Mts. faults. *Annals of Geophysics, 46*,(5). https://doi.org/10.4401/ag-3457.

Gatto, P., & Carbognin, L. (1981). The lagoon of Venice: Natural environmental trend and man-induced modification, *Hydrol. Sci. Bull., 26*(4), 379–391, https://doi.org/10.1080/02626668109490902.

Geurts, A.H., Cowie, P. A., Duclaux, G., Gawthorpe, R. L., Huismans, R. S., Pedersen, V. K., Wedmore, L. N. J. (2018). Drainage integration and sediment dispersal in active continental rifts: A numerical modelling study of the central Italian Apennines, *Basin Research*, *30*(5), 965-989, https://doi.org/10.1111/bre.12289.

Giacomuzzi, G., Chiarabba, C., De Gori, P. (2011). Linking the Alps and Apennines subduction systems: New constraints revealed by high-resolution teleseismic tomography. *Earth Planet. Sci. Lett. 301*, 531–543, https//doi.org/10.1016/j.epsl.2010.11.033.

Gianelli, G., Manzella, A., & Puxeddu, M. (1997). Crustal models of the geothermal areas of southern Tuscany (Italy). *Tectonophysics, v. 281*, 3-4, p. 221-239, https://doi.org/10.1016/S0040-1951(97)00101-7.

Giunchi, C., Sabadini, R., Boschi, E., & Gasperini, P. (1996). Dynamic models of subduction: geophysical and geological evidence in the Tyrrhenian Sea. *Geophys. J. Int.,* 126, p. 555-578, https://doi.org/10.1111/j.1365-246X.1996.tb05310.x.

Gourmelen, N. & Amelung, F., (2005). Postseismic Mantle Relaxation in the Central Nevada Seismic Belt. *Science, 310*, 1473-1476. https://doi.org/10.1126/science.1119798.

Hammond, W.C., Blewitt, G. & Kreemer, C. (2016). GPS Imaging of vertical land motion in California and Nevada: Implications for Sierra Nevada uplift. *J. Geophys. Res. - Solid Earth*, 121, 10, 7681-7703, https://doi.org/10.1002/2016JB013458.

Hammond, W. C., Kreemer, C., Zaliapin, I., & Blewitt, G. (2019). Drought-triggered magmatic inflation, crustal strain, and seismicity near the Long Valley Caldera, Central Walker Lane. *J. Geophys. Res.- Solid Earth, 124*, https://doi.org/ 10.1029/2019JB017354.

Haskell, N.A., (1935). The motion of a viscous fluid under a surface-load with particular reference to the Pleistocene ice-sheets, *Eos, 16*(1), p.104, https://doi.org/10.1029/TR016i001p00104-1.

Hoggard, M., White, N., Al-Attar, D (2016). Global dynamic topography observations reveal limited influence of large-scale mantle flow. *Nature Geosci.*, *9*, 456–463, https://doi.org/10.1038/ngeo2709.

Howell, A., Jackson, J., Copley, A. A., McKenzie, D., & Nissen, E. (2017). Subduction and vertical coastal motions in the eastern Mediterranean. *Geophys. J. Int., 211*, 593–620, https://doi.org/10.1093/gji/ggx307.

Isaia, R., Marianelli, P., & Sbrana, A., (2009). Caldera unrest prior to intense volcanism in Campi Flegrei (Italy) at 4.0 ka B.P.: Implications for caldera dynamics and future eruptive scenarios. *Geophys. Res. Lett., 36*(21), L21303, https://doi.org/10.1029/2009GL040513.

Kligfield, R., (1979). The Northern Apennines as a collisional orogen. *J. Sci., 279*, 676-691, https://doi.org/10.2475/ajs.279.6.676.

997 Kreemer, C., Blewitt, G. & Klein, E. C. (2014), A geodetic plate motion and Global Strain Rate
998 Model, *Geochem. Geophys. Geosyst., 15*, 3849–3889,
999 https://doi.org/10.1002/2014GC005407.
1000 Kreemer, C., Blewitt, G. & Davis, P.M. (2020). Geodetic evidence for a buoyant mantle plume
1001 beneath the Eifel volcanic area. NW Europe, EarthArXiv, https://eartharxiv.org/yab5d/.
1002 Lambeck, K., Smither, C. & Johnston, P. (1998). Sea-level change, glacial rebound and mantle
1003 viscosity for northern Europe. *Geophys. J. Int., 134*, 102–144, https://doi.org/10.1046/j.1365-
1004 246x.1998.00541.x
1005 Luthcke, S.B., Sabaka, T.J. Loomis, B.D., Arendt, A.A., McCarthy, J.J. & Camp, J. (2013).
1006 Antarctica, Greenland and Gulf of Alaska land ice evolution from an iterated GRACE global
1007 mascon solution. *J. Glac. 59*(216), 613-631, https://doi.org/10.3189/2013JoG12J147.
1008 Malinverno, A. & Ryan, W.B.F. (1986). Extension in the Tyrrhenian Sea and shortening in the
1009 Apennines as result of arc migration driven by sinking of the lithosphere. *Tectonics*, *v. 5*, n.
1010 2, p 227-245, https://doi.org/10.1029/TC005i002p00227.
1011 Mancini, M., D'Anastasio, E., Barbieri, M., & De Martini, P. M. (2007). Geomorphological,
1012 paleontological and $^{87}Sr/^{86}Sr$ isotope analyses of early Pleistocene paleoshorelines to define
1013 the uplift of Central Apennines (Italy). *Quaternary Res. 67*, p. 487–501,
1014 https://doi.org/10.1016/j.yqres.2007.01.005.
1015 Marinelli, G., Barberi, F., & Cioni, R. (1993). Sollevamenti neogenici e intrusioni acide della
1016 Toscana e del Lazio settentrionale. *Mem. Soc. Geol. It., 49*, 279–288.
1017 Martini, I.P., & Sagri, M. (1993). Tectono-sedimentary characteristics of Late Miocene-
1018 Quaternary extensional basins of the Northern Apennines, Italy. *Earth-Science Reviews,*
1019 *34*(3), 197-233, ISSN 0012-8252, https://doi.org/10.1016/0012-8252(93)90034-5.
1020 McKenzie, D., (1978). Some remarks on the development of sedimentary basins. *Earth planet.*
1021 *Sci. Lett., 40*(1), 25–32, https://doi.org/10.1016/0012-821X(78)90071-7.
1022 McKenzie, D., Jackson, J., & Priestley, K., (2005). Thermal structure of oceanic and continental
1023 lithosphere. *Earth planet. Sci. Lett.,* 233(3), 337– 349,
1024 https://doi.org/10.1016/j.epsl.2005.02.005.
1025 Mueller, K., Kier, G., Rockwell, T. & Jones, C. H. (2009). Quaternary rift flank uplift of the
1026 Peninsular Ranges in Baja and southern California by removal of mantle lithosphere.
1027 *Tectonics, 28,* TC5003, https://doi.org/10.1029/2007TC002227.
1028 Oldow, J. S., Ferranti, L., Lewis, D. S., Campbell, J. K., D'Argenio, B., Catalano, R., Pappone,
1029 G., Carmignani, L., Conti, P., & Aiken, C. L. V. (2002). Active fragmentation of Adria, the
1030 north African promontory, central Mediterranean. *Geology, v. 30*, n. 9, p. 779-782,
1031 https://doi.org/10.1130/0091-7613(2002)030<0779:AFOATN>2.0.CO;2.
1032 Ori, G. G., Serafini, G., Visentini, G., Lucchi, F. R., Casnedi, R., Colalongo, M. L. & Mosna, S.,
1033 (1993). Depositional history of the Pliocene-Pleistocene Adriatic foredeep (Central Italy)
1034 from surface and subsurface data, *in Generation, Accumulation and Production of Europe's*
1035 *Hydrocarbon III,* pp. 233–258, ed. Specer, A.M., Spec. Publ., Eur. Ass. Petr. Geosc., 3.
1036 Pace, P., Scisciani, V., Calamita, F., Butler, R. W. H., Iacopini, D., Esestime, P., Hodgson, N.,
1037 (2015). Inversion structures in a foreland domain: Seismic examples from the Italian
1038 Adriatic Sea. *Interpretation,* https://dx.doi.org/10.1190/INT-2015-0013.1
1039 Patacca, E., & Scandone, P., (1989). Post-Tortonian mountain building in the Apennines. The
1040 role of the passive sinking of a relic lithospheric slab, *in* Boriani, A., Bonafede, M., Piccardo,
1041 G.B., and Vai, G.B., eds., *The Lithosphere in Italy: Atti dei Convegni Lincei, v. 80*, p. 157–
1042 176.

Peltier, W. R. (2004). Global glacial isostasy and the surface of the ice-age Earth: The ICE-5G (VM2) model and GRACE. *Annu. Rev. Earth Planet. Sci., 32*(1), 111–149, https://doi.org/10.1146/annurev.earth.32.082503.144359.

Peltier, W. R., Argus, D. F. & Drummond, R. (2015). Space geodesy constrains ice age terminal deglaciation: The global ICE-6G_C (VM5a) model. *J. Geophys. Res. - Solid Earth*, 120, 450–487, https://doi.org/10.1002/2014JB011176.

Piana Agostinetti, N., & Amato, A. (2009). Moho depth and V_p/V_s ratio in peninsular Italy from teleseismic receiver functions. *J. Geophys. Res., 114,* B06303, https://doi.org/10.1029/2008JB005899.

Piromallo, C., & Morelli, A. (2003). *P* wave tomography of the mantle under the Alpine-Mediterranean area. *J. Geophys. Res., 108(*B2), 2065, https://doi.org/10.1029/2002JB001757.

Pizzi, A. (2003). Plio-Quaternary uplift rates in the outer zone of the central Apennines fold-and-thrust belt, Italy. *Quaternary International, v. 101–102*, p. 229-237, https://doi.org/10.1016/S1040-6182(02)00105-2.

Rebischung, P., Altamimi, Z., Ray, J., & Garayt, B. (2016). The IGS contribution to ITRF2014. *J. Geod., 90,* 7, 611–630, https://doi.org/10.1007/s00190-016-0897-6.

Reilinger, R. (1986). Evidence for postseismic viscoelastic relaxation following the 1959 M- 7.5 Hebgen Lake, Montana, earthquake. *J. Geophys. Res, v. 91*(B9), 9488-9494, https://doi.org/10.1029/JB091iB09p09488.

Riguzzi, F., Crespi, M., Devoti, R., Doglioni, C., Pietrantonio, G. Pisani A.R. (2013). Strain rate relaxation of normal fault and thrust faults in Italy. *Geophys. J. Int.*, https://doi.org/10.1093/gji/ggt304.

Rovida A., Locati M., Camassi R., Lolli B., Gasperini P. (eds), 2019. Italian Parametric Earthquake Catalogue (CPTI15), version 2.0. Istituto Nazionale di Geofisica e Vulcanologia (INGV). https://doi.org/10.13127/CPTI/CPTI15.2.

Royden, L., Patacca, E., & Scandone, P. (1987). Segmentation and configuration of subducted lithosphere in Italy: An important control on thrust-belt and foredeep-basin evolution. *Geology, 15,* 714-717, https://doi.org/10.1130/0091-7613(1987)15<714:SACOSL>2.0.CO;2.

Savage, J. C., Gan, W., & Svarc, J. L. (2001). Strain accumulation and rotation in the Eastern California Shear Zone. *J. Geophys. Res. - Solid Earth*, *106*(B10), 21,995–22,007, https://doi.org/10.1029/2000JB000127.

Sen, P. K. (1968). Estimates of the regression coefficient based on Kendall's tau. *J. Am. Stat. Assoc., 63,* 1379–1389.

Serpelloni, E., Anzidei, M., Baldi, P., Casula G., & Galvani, A. (2005). Crustal velocity and strain-rate fields in Italy and surrounding regions: new results from the analysis of permanent and non-permanent GPS networks. *Geophys. J. Int., 161*, 861–880, https://doi.org/10.1111/j.1365-246X.2005.02618.x.

Serpelloni, E., Faccenna, C., Spada, G., Dong, D. & Williams, S. D. P. (2013). Vertical GPS ground motion rates in the Euro-Mediterranean region: New evidence of velocity gradients at different spatial scales along the Nubia-Eurasia plate boundary. *J. Geophys. Res., 118,* https://doi.org/10.1002/2013JB010102.

Serri, G., Innocenti, F., & Mentti, P., (1993). Geochemical and petrological evidence of the subduction of delaminated Adriatic continental lithosphere in the genesis of the Neogene-Quaternary magmatism of central Italy, *Tectonophysics*, *223*(1), 117-147, https://doi.org/10.1016/0040-1951(93)90161-C.

Shaw, M., & Pysklywec, R. (2007). Anomalous uplift of the Apennines and subsidence of the Adriatic: The result of active mantle flow? *Geophys. Res. Lett., 34*, L04311, https://doi.org/10.1029/2006GL028337.
Silverii, F., D'Agostino, N., Métois, M., Fiorillo, F., & Ventafridda, G. (2016). Transient deformation of karst aquifers due to seasonal and multiyear groundwater variations observed by GPS in southern Apennines (Italy). *J. Geophys. Res. - Solid Earth*, *121*, 8315–8337 https://doi.org/10.1002/2016JB013361.
Spakman, W., van der Lee, S., & van der Hilst, R. (1993). Travel-time tomography of the European-Mediterranean mantle down to 1400 km. *Phys. Earth Planet. Inter., 79*, 3–74.
Stern, T. A., & Ten Brink, U. S. (1989). Flexural uplift of the Transantarctic Mountains. *J. Geophys. Res., 94,* 10,315–10,330, doi:10.1029/JB094iB08p10315.
Stucchi, M., Meletti, C., Montaldo, V., Crowley, H., Calvi, G. M., & Boschi, E. (2011). Seismic hazard assessment (2003–2009) for the Italian building code. *Bull. Seismol. Soc. Am.*, *101*, 1885–1911, https://doi.org/10.1785/0120100130.
Theil, H. (1950). A rank-invariant method of linear and polynomial regression analysis. *Indag. Math., 12,* 85–91.
Thompson, G. A. & Parsons, T. (2009). Can footwall unloading explain late Cenozoic uplift of the Sierra Nevada crest? *Int. Geol. Rev., 51,* 9, 986-993, https://doi.org/10.1080/00206810903059156.
Tosi, L., Carbognin, L., Teantini, P., Strozzi, T., & Wegmüller, U. (2002), Evidence of the present relative land stability of Venice, Italy, from land, sea, and space observations. *Geophys. Res. Lett., 29*(12), 1562, https://doi.org/10.1029/2001GL013211.
Turcotte, D.L., & Schubert, G. (2002). Geodynamics, 2nd Edition, Cambridge University Press.
Vening Meinesz, F.A., (1937). The determination of the Earth's plasticity from the postglacial uplift of Scandinavia: isostatic adjustment. *Kon. Akad. Wettensch, 40*, 654–662.
Vening Meinesz, F. A. (1950). Les graben africains, résultat de compression ou de tension dans la croûte terrestre? *Inst. R. Colon. Belge Bull., 21*, 539 – 552.
Watkins, M. M., Wiese, D. N., Yuan, D.-N. Boening, C. & Landerer, F. W. (2015). Improved methods for observing Earth's time variable mass distribution with GRACE using spherical cap mascons. *J. Geophys. Res. - Solid Earth, 120*(4), 2648-2671, https://doi.org/10.1002/2014JB011547.
Wdowinski, S., Bock, Y., Zhang, J., Fang, P., Genrich, J., (1997). Southern California Permanent GPS Geodetic Array: Spatial filtering of daily positions for estimating coseismic and postseismic displacements induced by the 1992 Landers earthquake, *J. Geophys. Res. - Solid Earth, 102*(B8), 18,057-18070, https://doi.org/10.1029/97JB01378.
Weissel, J. K., & Karner, G. D. (1989). Flexural uplift of rift flanks due to mechanical unloading of the lithosphere during extension. *J. Geophys. Res., 94,* 13,919 – 13,950, https://doi.org/10.1029/JB094iB10p13919.
Wessel, P., Smith, W. H. F., Scharroo, R., Luis, J. F., & Wobbe, F. (2013). Generic Mapping Tools: Improved version released. *Eos, Trans. Am. Geophys. Union, 94(45*), 409–410. https://doi.or g/10.1002/2013EO450001.
Wiese, D. N., Landerer, F. W. & Watkins, M. M. (2016). Quantifying and reducing leakage errors in the JPL RL05M GRACE mascon solution. *Water Resour. Res., 52*, 7490–7502, https://doi.org/10.1002/2016WR019344.

Wortel, M.J.R., & Spakman, W. (2000). Subduction and slab detachment in the Mediterranean-Carpathian region. *Science, v. 290*, p. 1910-1917, https://doi.org/10.1126/science.290.5498.1910.

Zhu, H., Bozdag, E., Peter, D., & Tromp, J. (2012). Structure of the European upper mantle revealed by adjoint tomography. *Nat. Geosci., 5*, 493–498, https://doi.org/10.1038/ngeo1501

Figures and Captions

Figure 1

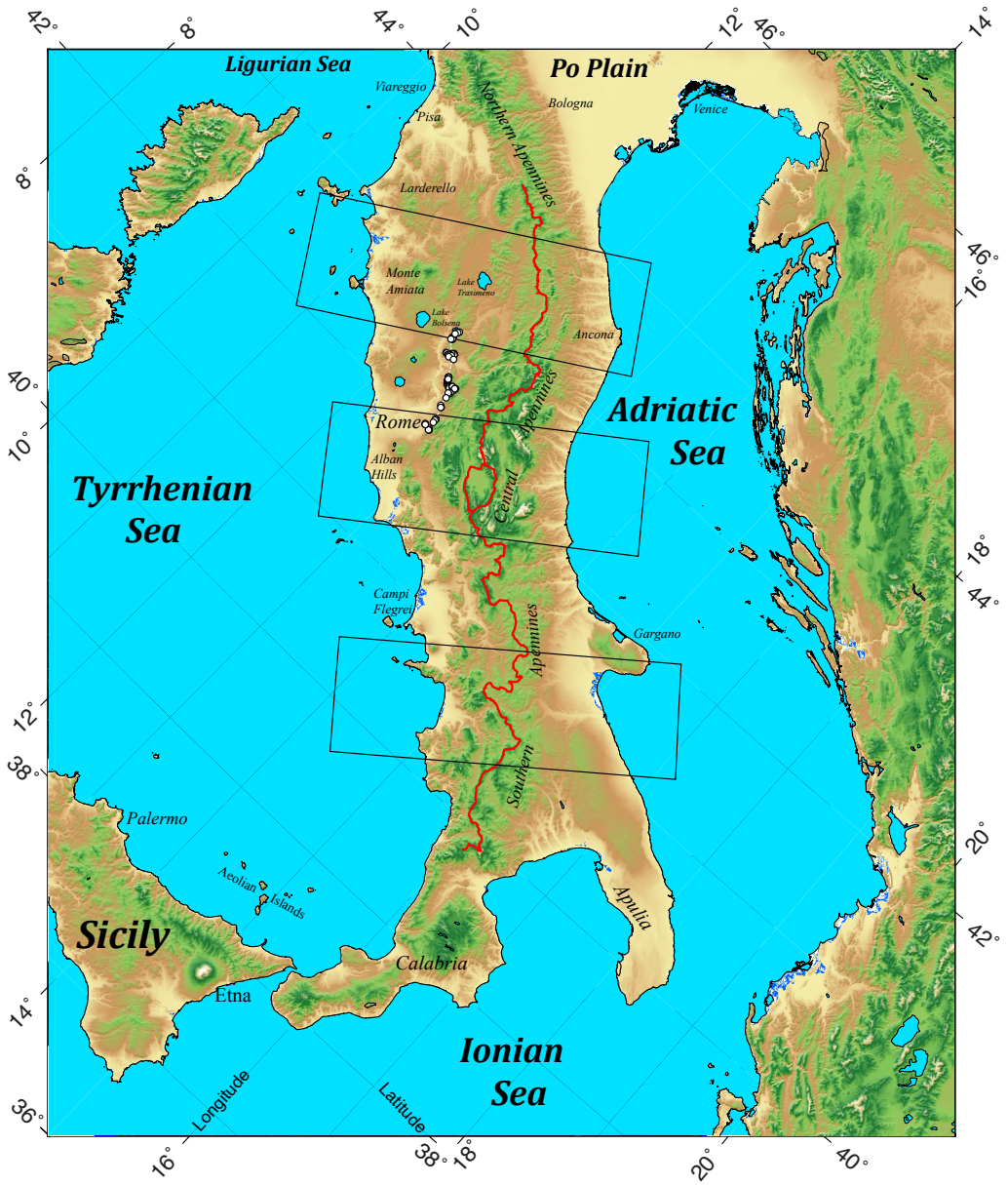

Figure 1. Color shaded topography of Apennines, Italy and nearby locations. Red line indicates location of topographic drainage divide along the crest of the Apennines. Black rectangles indicate location of three profiles extending from Tyrrhenian to Adriatic seas used in later figures. White circles with black outline connected by white dashed line depict the location of observed Pleistocene shoreline of Mancini et al., (2007).

Figure 2.

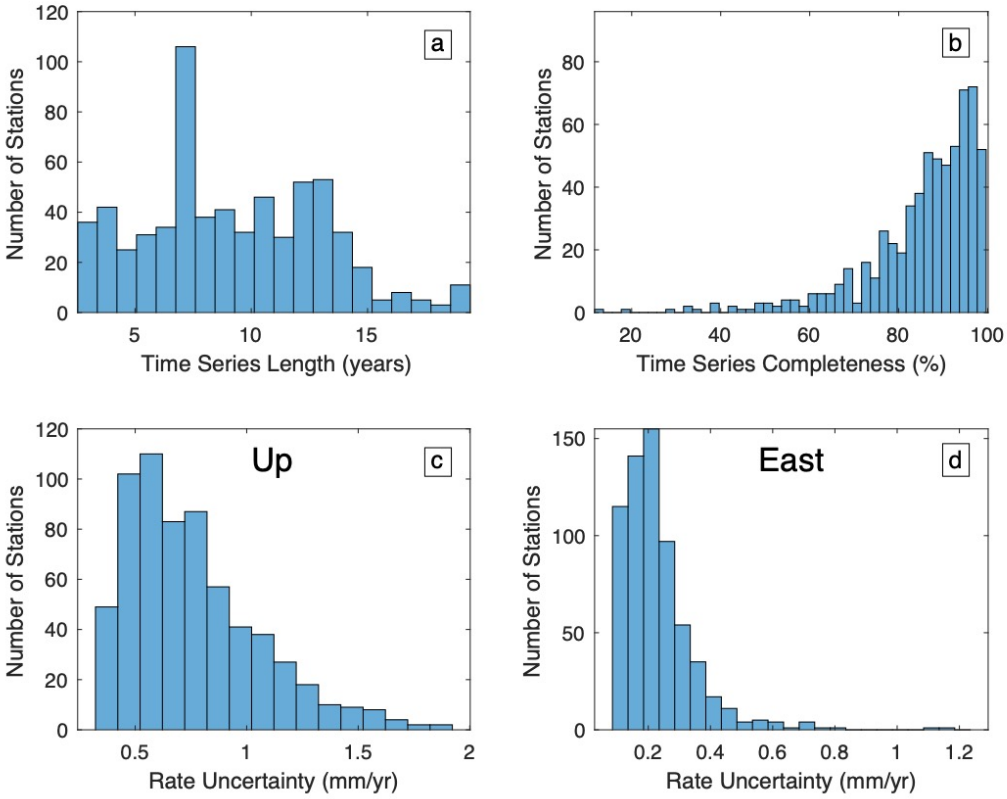

Figure 2. Statistics of time series that are used in the GPS Imaging. a) Histogram of time series duration in years. b) Histogram of completeness of time series, where 100% indicates there are no data gaps between first and last observation. c) Histogram of the uncertainty of the MIDAS rates from the vertical time series. d) Histogram of the uncertainty of the MIDAS east rate, which is similar to that or the north rate (but is not shown).

Figure 3.

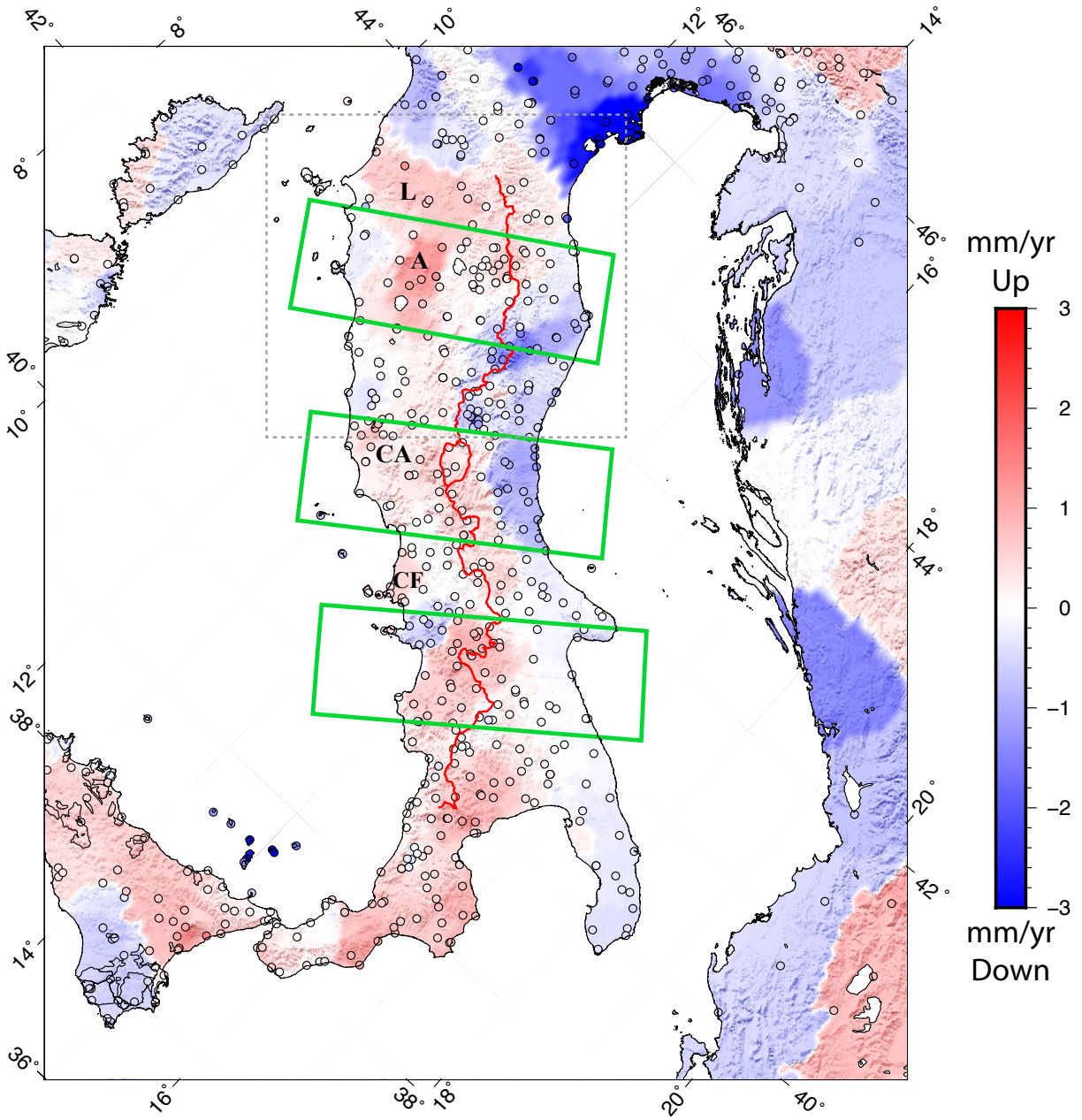

Figure 3. Result of GPS Imaging of vertical rate for Italy and surrounding regions, corrected for the effects of GIA. Color scale is in mm/yr, red upward, blue downward. Circles indicate location of GPS stations. Color of each station circle indicates the median filtered vertical rate value for the station. Green rectangles indicate location of velocity profiles. Labels indicate locations discussed in text, L, Larderello; A, Amiata; CA, Colli Albani; CF, Campi Flegrei.

Figure 4.

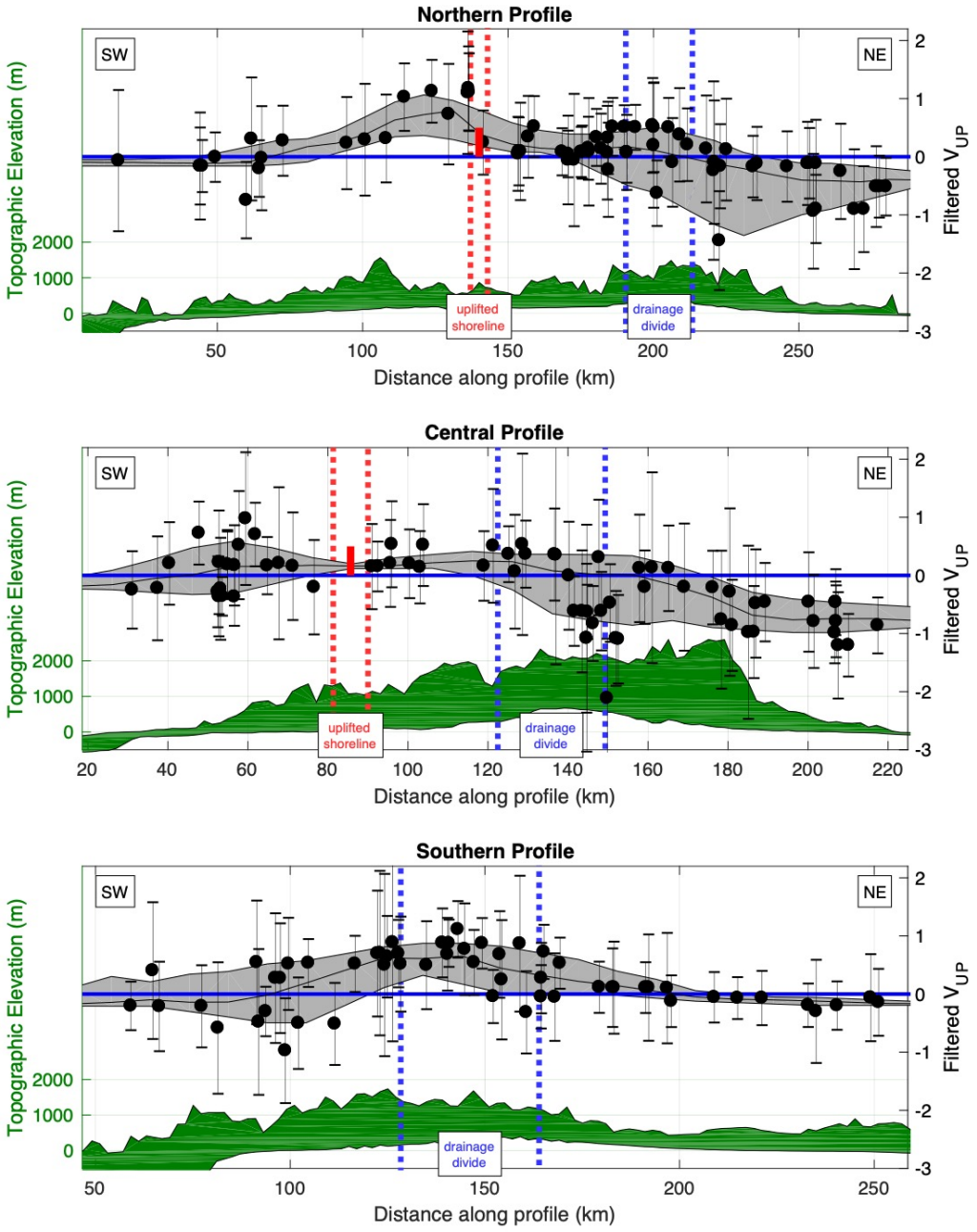

Figure 4. Profiles of vertical GPS velocity as a function of distance across three profiles whose locations are shown in Figures 1 and 3, where top is northern, middle is central, and bottom is southern profile. Black circles are values of median filtered GPS velocities and error bars with their 1-sigma uncertainties. The gray band behind indicates a smoothed envelope of the GPS Imaging vertical rate field, with the black line showing its median value within the profile rectangle. The green profile beneath the GPS values indicates the envelope of minimum to maximum elevation across the profile. The location of the drainage divide is shown with vertical blue dashed lines. The location of the Early Pleistocene uplifted shoreline (D'Agostino et al., 2001b) is indicated with a vertical short red bar whose length corresponds to the range of rates between 0 to 0.5 mm/yr. The dashed red lines indicate the extent of the shoreline within the profile rectangle.

Figure 5.

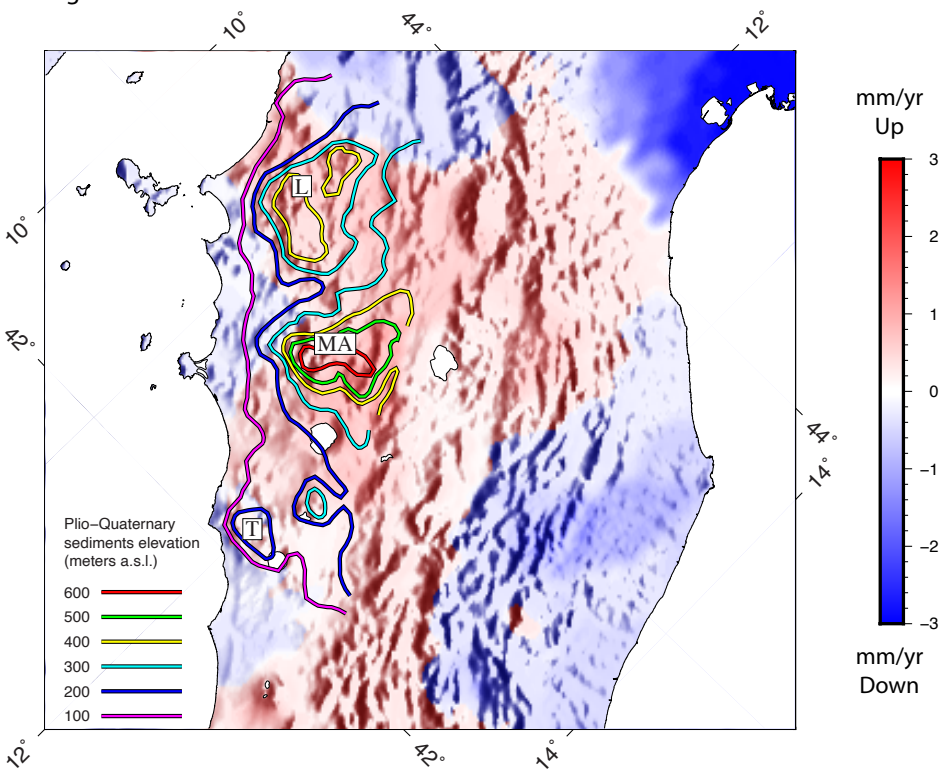

Figure 5. GPS imaging of vertical velocity field (same as Figure 3) and contours of elevation of Neogene marine sediments (Lower Pliocene-Quaternary) from Marinelli et al. (1993) showing the correlation between the vertical geodetic signal with regions of long-term Neogene vertical land motion and geothermal fields characterized by Quaternary magmatic intrusions (L, Larderello; MA, Monte Amiata; T, Monti della Tolfa).

Figure 6.

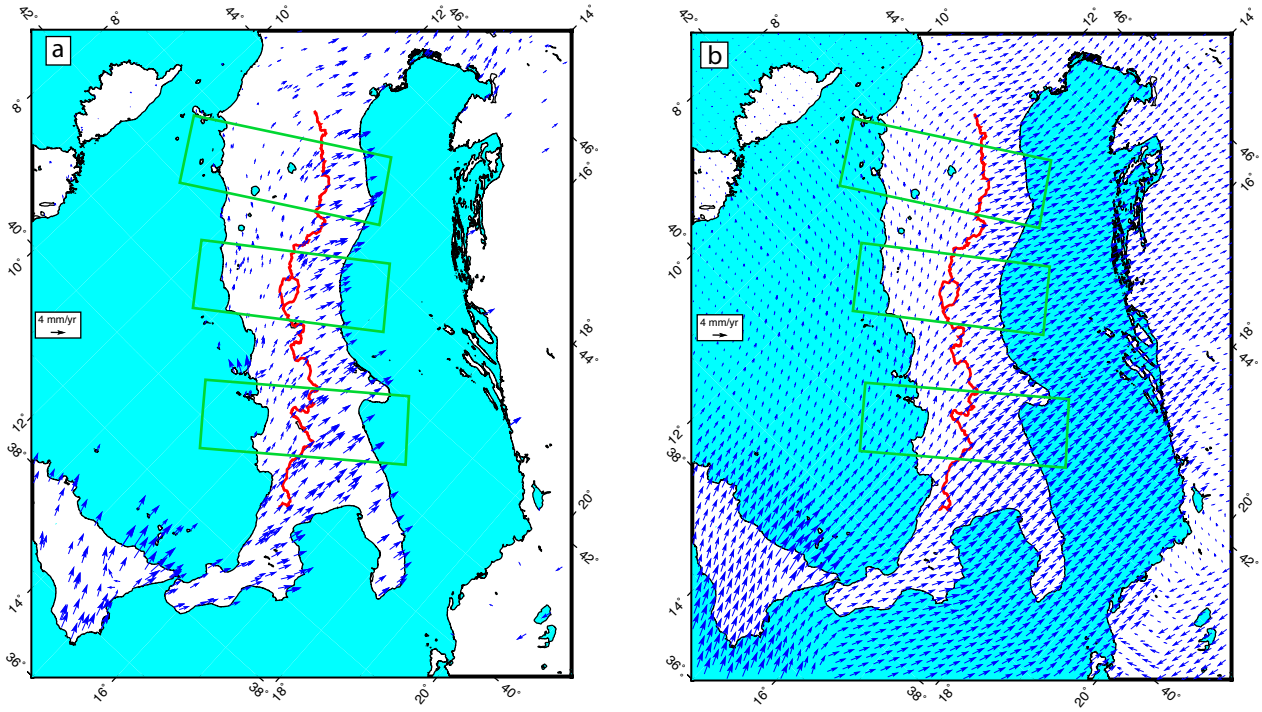

Figure 6. a) Median spatial filtered horizontal MIDAS GPS velocities from GPS time series in Eurasian reference frame. b) Gridded horizontal GPS velocity obtained using GPS Imaging. Other map elements are the same as in previous figures.

Figure 7.

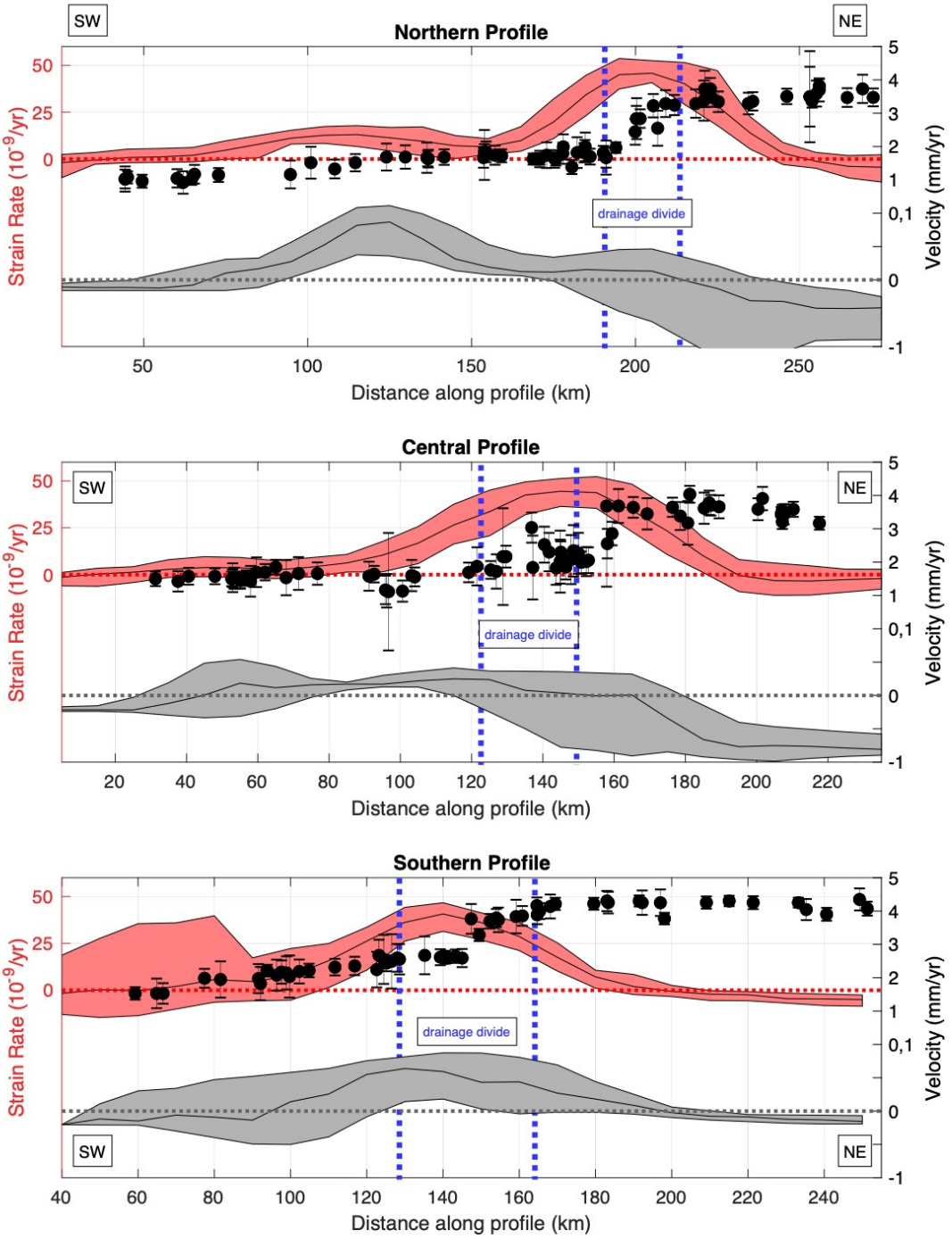

Figure 7. For same profiles shown in Figure 4, black circles indicate magnitude of median spatial filtered GPS velocity with 1-sigma uncertainty bars. Salmon color indicates smoothed envelope of dilatational strain rate estimated from gridded horizontal velocity field shown in Figure 6. The gray band indicates the same smoothed envelope of the vertical rate from Figure 4, with the black line indicating its median value. The location of the drainage divide is shown with vertical blue dashed lines. The horizontal dotted salmon and gray colored lines indicate zero strain rate and vertical rate, respectively.

Figure 8.

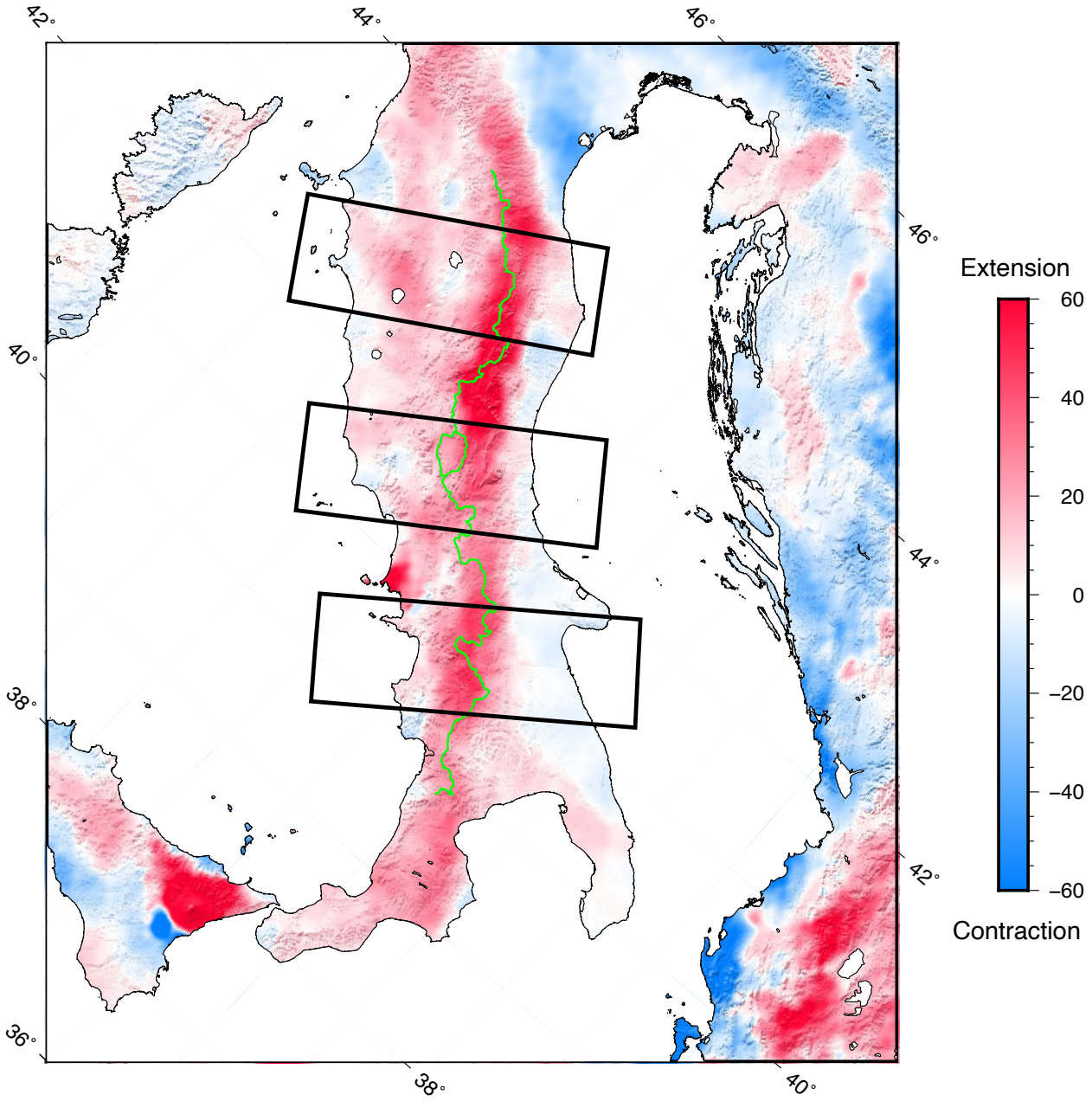

Figure 8. Map of dilatational component of strain rate derived from horizontal velocity field using GPS Imaging and a Gaussian averaging window of width w = 8 km (see supplemental materials). Color scale indicates value of strain rate in units of nanostrains/year, extensional in magenta color, contraction in cyan. Green line is drainage divide as in previous map figures.

Figure 9.

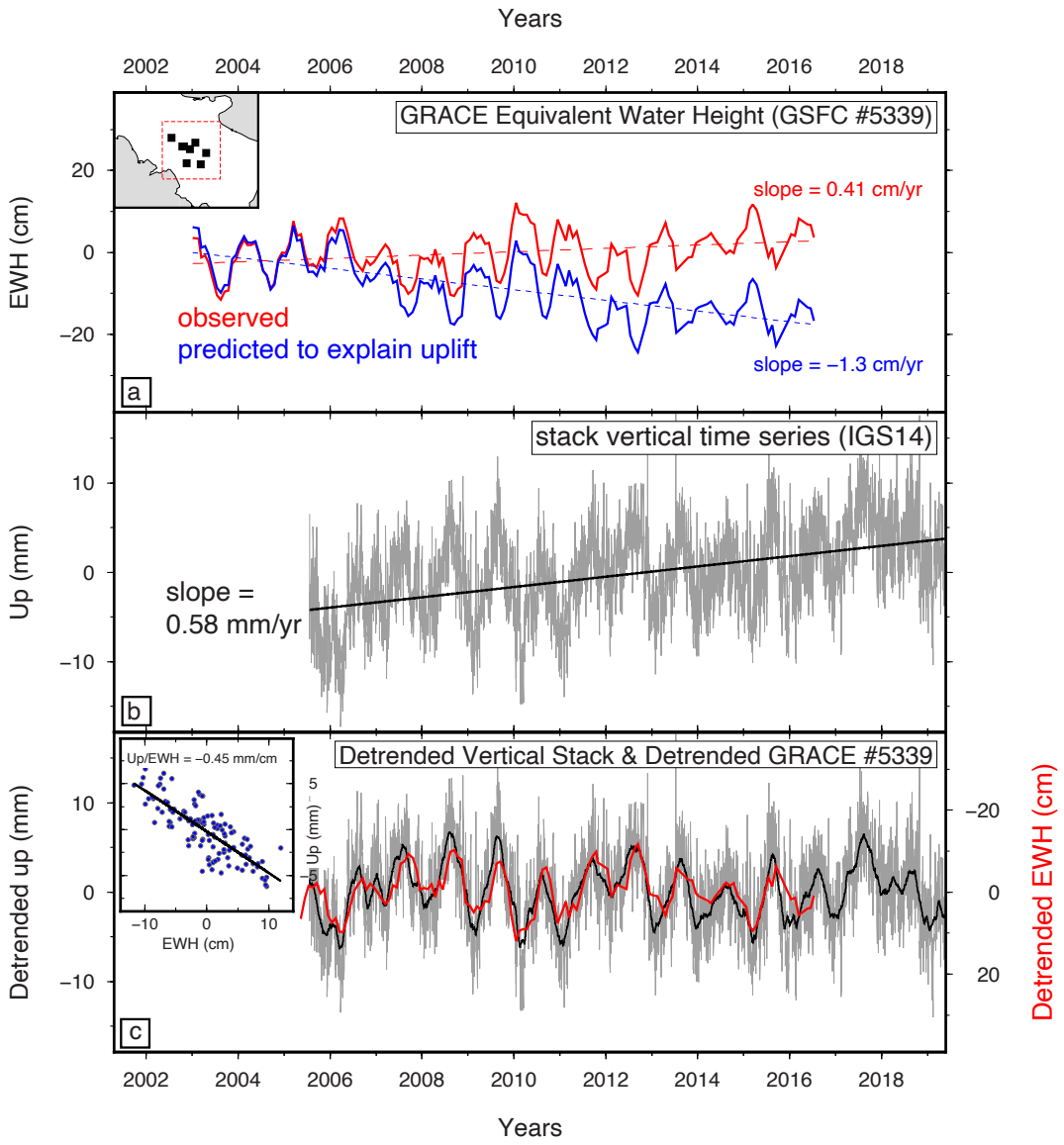

Figure 9. Analysis of hydrological forcing. a) Monthly equivalent water height (EWH) time series from GRACE (GSFC solution mascon #5339). The red line is the observed value together with the best-fit trend (dashed) showing weak increasing water loading. The blue line shows the same time series after detrending and addition of the trend required to explain the observed uplift in the case of hydrological loading. The inset shows the geographical location of the mascon. b) Stack of selected GPS vertical time series (stations shown in the inset of a)) and associated best-fit trend showing mean uplift rate of 0.58 mm/yr. c) Comparison between the detrended GRACE EWH observations (red) and detrended stacked vertical GPS positions (resampled at GRACE observation times, in black). The inset shows the regression between vertical displacement (Up) and EWH, giving a relation of -0.43 mm uplift per cm of EWH. This relation was used to calculate the predicted hydrologically-driven uplift rate shown in a), (see text for details). The disagreement of trends in a) illustrate that Apennine uplift is not attributable to hydrological loading.

Figure 10.

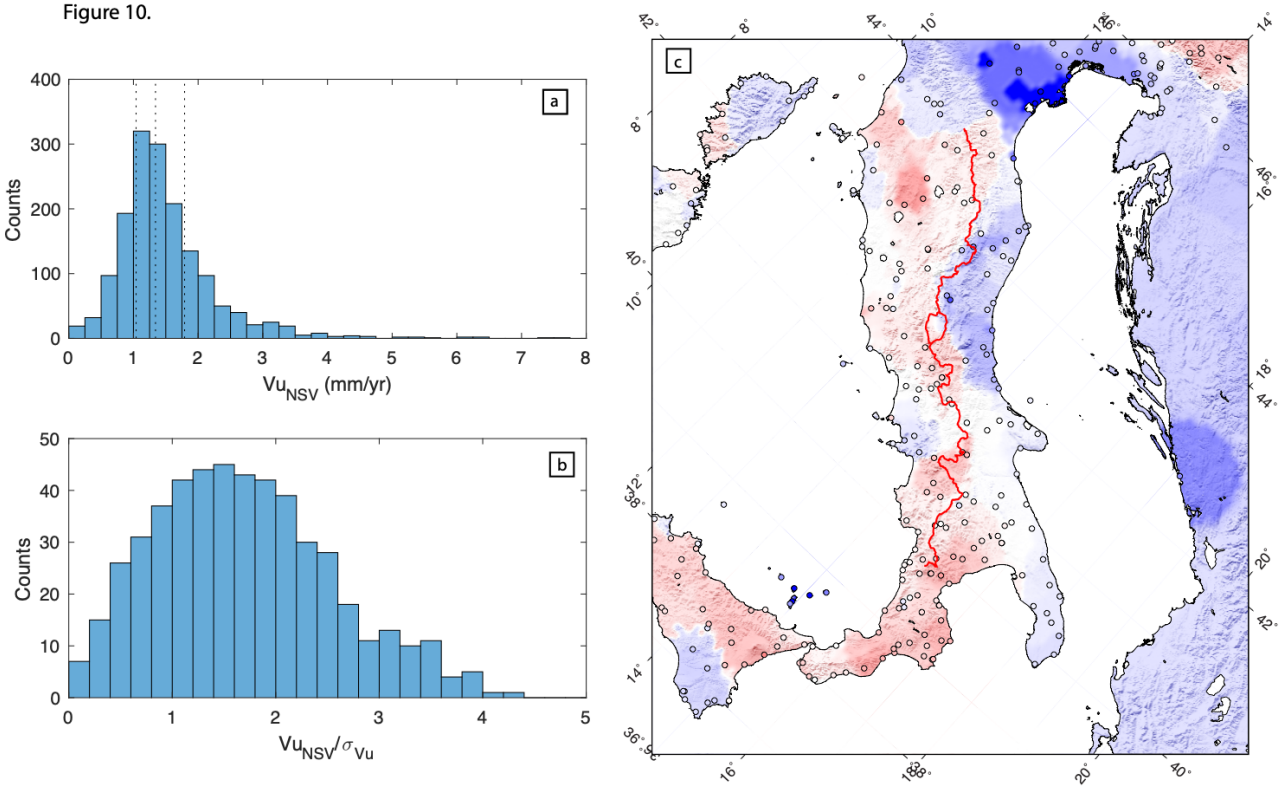

Figure 10. a) Histogram of vertical velocity variability index $V_{u,NSV}$. Vertical dotted lines indicate 25th, 50th, and 75th percentiles of the distribution. b) Histogram of the vertical velocity variability index divided by the uncertainty in the MIDAS vertical rate ($V_{u,NSV}/\sigma_{Vu}$) indicates a minority of velocities are have variability that is significantly different than the MIDAS rate. c) GPS Imaging of vertical velocity using only the subset of velocities that have variability below the median value of $V_{u,NSV}$ = 1.8 mm/yr.

Figure 11.

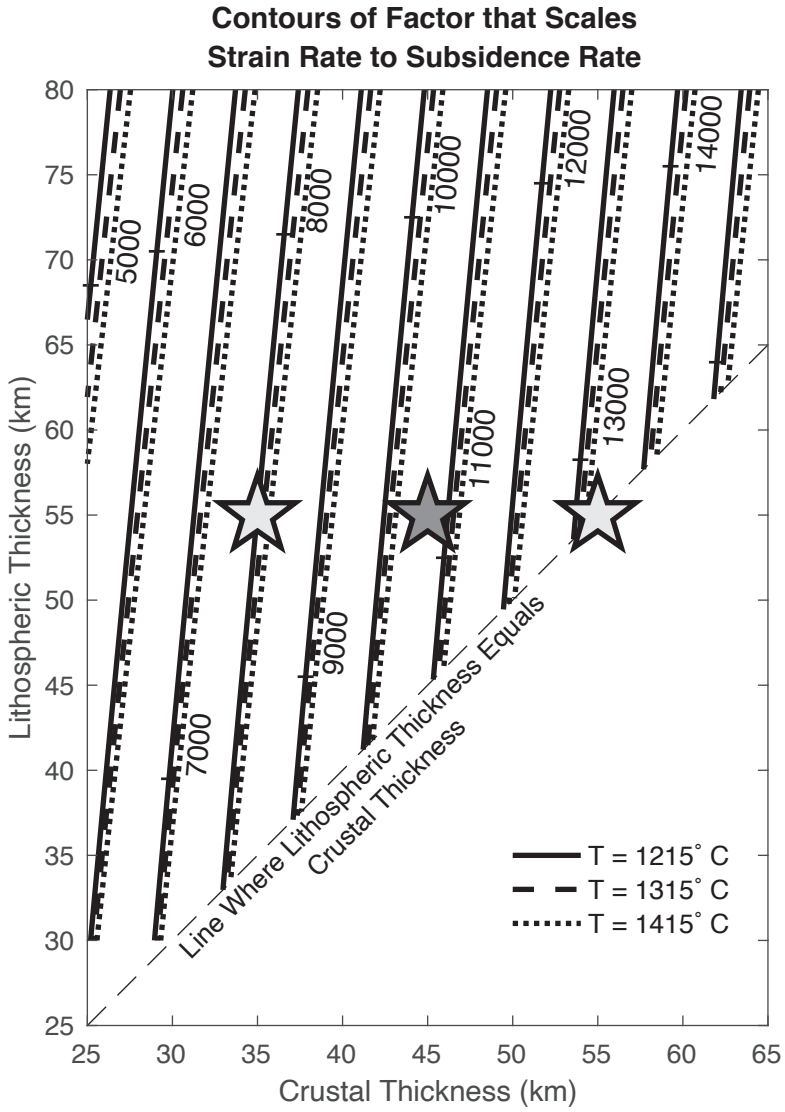

Figure 11. Contours of the scale factor predicting vertical subsidence rate expected from a given dilatational strain rate. The factor is calculated using equation (2) from Howell et al., (2017) for various values of crustal (t_c) and lithospheric (t_l) thickness and asthenospheric temperature T_1 (see text for details). Grey stars indicate value for t_c = 35, 45 and 55 km and lithospheric thickness t_l = 55 km.

Figure 12.

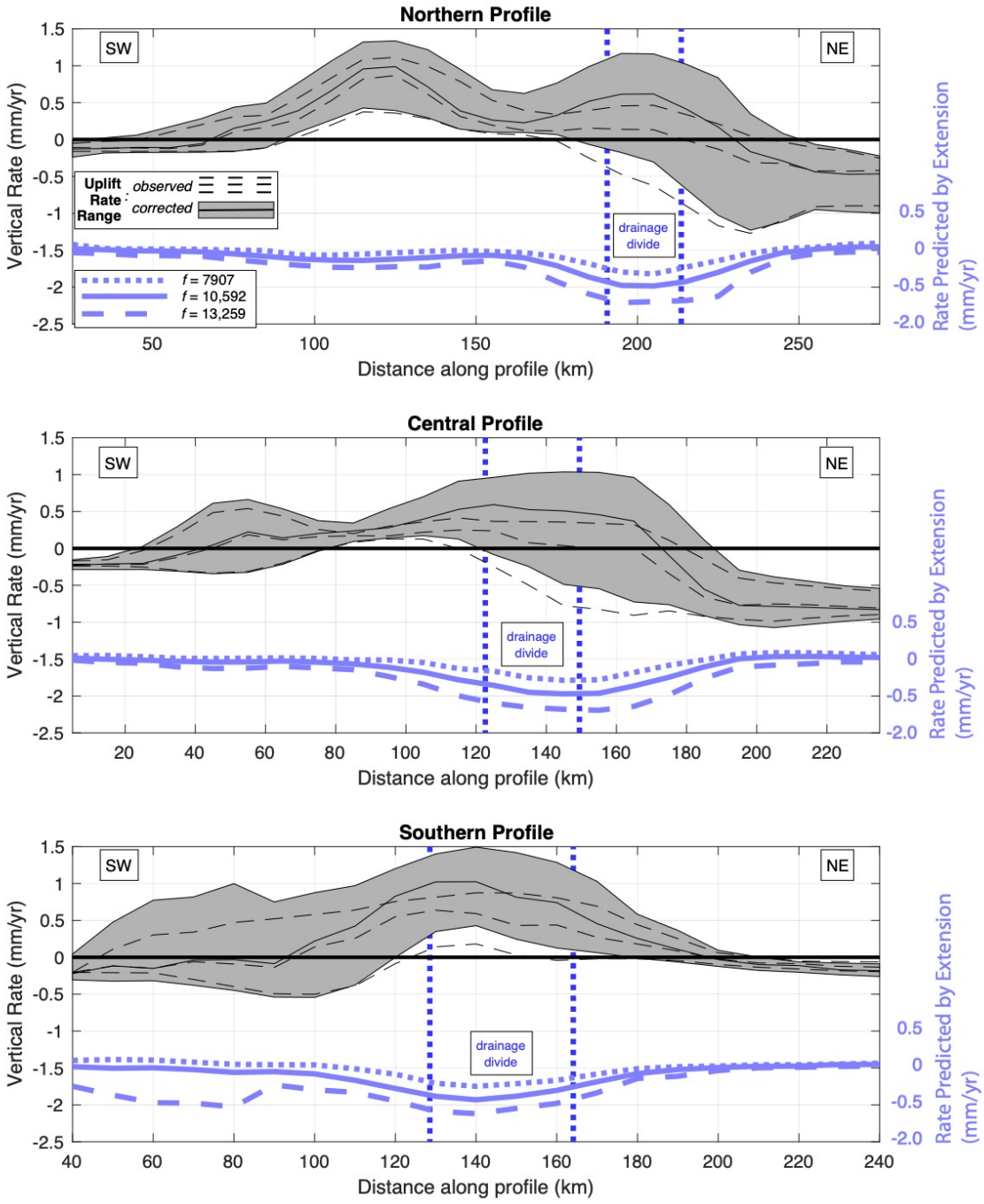

Figure 12. Estimated vertical rate of the mantle upwelling beneath the Apennines. We correct the imaged vertical rate field (dashed black lines are from Figure 4) for the rate expected from subsidence associated with crustal extension. For the same profiles as in previous figures, we use the scale factors of f=7907, 10,592, and 13,259 (from the location of stars in Figure 11) to predict the subsidence rates (dotted, solid, dashed purple lines respectively) from the geodetically observed dilatational strain rate. The predicted subsidence (negative vertical rate) is subtracted from the observed uplift rates so the corrected uplift rates (gray solid area) are greater than the uncorrected rates. Legend in a) applies to b) and c) as well.

Figure 13.

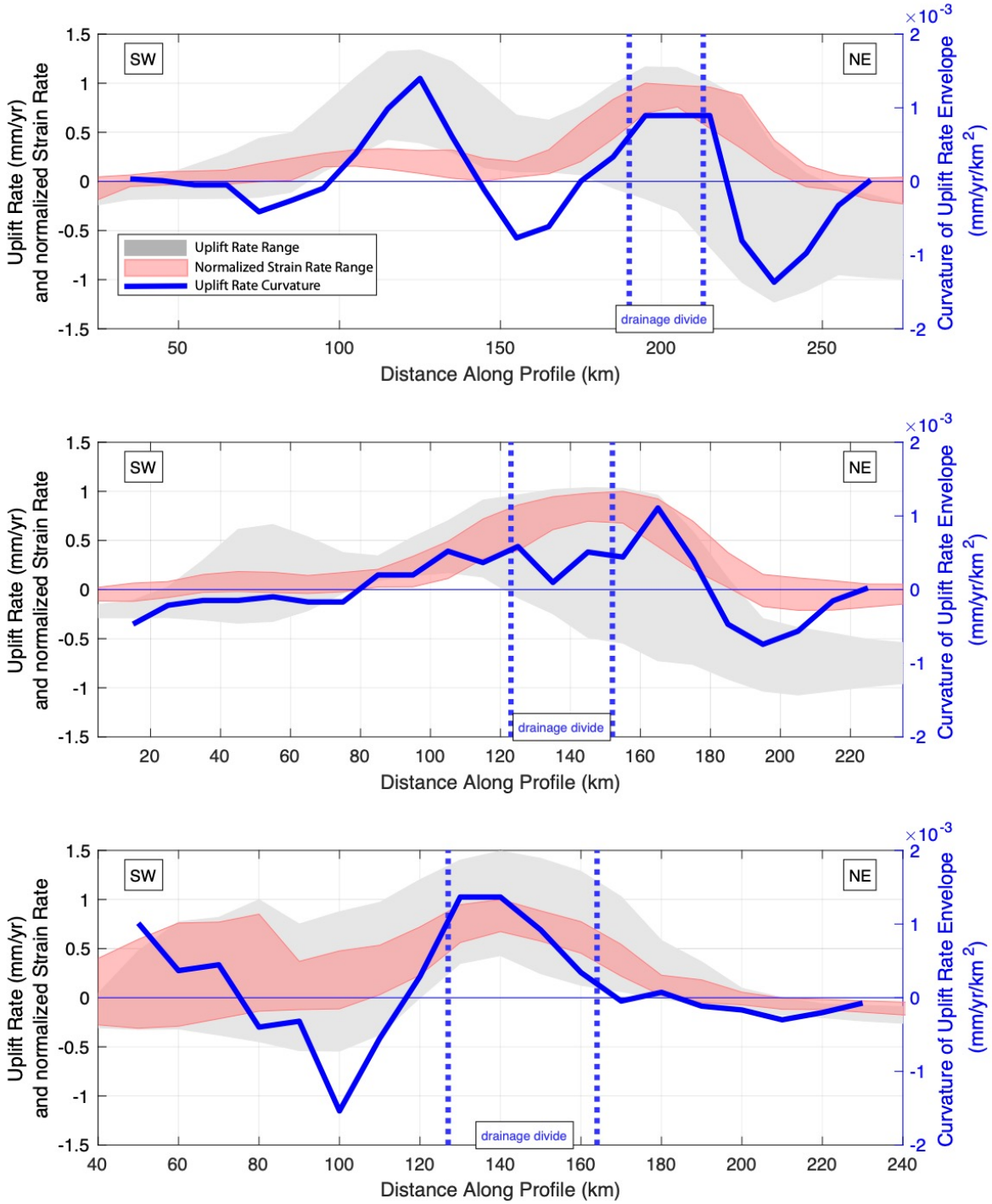

Figure 13. Median filtered profile of curvature (blue) of the uplift profile calculated with double finite difference of the uplift envelope. The sign has been changed so concave downward uplift signal curvature is shown with as positive second derivative. The uplift envelope (gray) is adjusted for thinning of the crust (Figure 12), and the strain envelope (salmon color) is from Figure 7. Location of drainage divide is shown as in previous figures.